# SIMULATION RESULTS OF AN INDUCTIVELY-COUPLED RF PLASMA

# TORCH IN TWO AND THREE DIMENSIONS FOR PRODUCING A METAL

# MATRIX COMPOSITE FOR NUCLEAR FUEL CLADDING

A Thesis

by

EDDIE FRANK (TREY) HOLIK III

December 2008

Major Subject: Physics

# SIMULATION RESULTS OF AN INDUCTIVELY-COUPLED RF PLASMA

# TORCH IN TWO AND THREE DIMENSIONS FOR PRODUCING A METAL

# MATRIX COMPOSITE FOR NUCLEAR FUEL CLADDING

A Thesis

by

EDDIE FRANK (TREY) HOLIK III

Submitted to the Office of Graduate Studies of
Texas A&M University
in partial fulfillment of the requirements for the degree of

MASTER OF SCIENCE

Approved by:

| | |
|---|---|
| Chair of Committee, | Peter M. McIntyre |
| Committee Members, | Alfred D. McInturff |
| | Lin Shao |
| Head of Department, | Edward S. Fry |

December 2008

Major Subject: Physics

# ABSTRACT

Simulation Results of an Inductively-Coupled RF Plasma Torch in Two and Three
Dimensions for Producing a Metal Matrix Composite for Nuclear Fuel Cladding.

(December 2008)

Eddie Frank (Trey) Holik III, B.S., Angelo State University

Chair of Advisory Committee: Dr. Peter M. McIntyre

I propose to develop a new method for the synthesis of metal matrix composites (MMC) using aerosol reactants in a radio frequency (RF) plasma torch. An inductively-coupled RF plasma torch (ICPT) may potentially be designed to maintain laminar flow and a radial temperature distribution. These two properties provide a method by which a succession of metal layers can be applied to the surface of SiC fibers. In particular, the envisaged method provides a means to fully bond any desired metal to the surface of the SiC fibers, opening the possibility for MMCs in which the matrix metal is a high-strength steel.

A crucial first step in creating the MMC is to test the feasibility of constructing an ICPT with completely laminar flow in the plasma region. In this work, a magnetohydrodynamic (MHD) model is used along with a computational fluid dynamic (CFD) software package called FLUENT$^©$ to simulate an ICPT. To solve the electromagnetic equations and incorporate forces and resistive heating, several user-defined functions (UDF) were written to add to the functionality of FLUENT$^©$. Initially, an azimuthally-symmetric, two-dimensional model was created to set a test baseline for operating in FLUENT$^©$ and to verify the UDF. To incorporate coil angle and current leads, a fully three dimensional model UDF was written. Preliminary results confirm the functionality of the code. Additionally, the results reveal a non-mixing, laminar flow outer region for an axis-symmetric ICPT.

**TABLE OF CONTENTS**

# LIST OF FIGURES

Page

## LIST OF TABLES

# I. INTRODUCTION: CONCEPTUAL MMC DESIGN

## A. Design Introduction

For the first time in 30 years plans are afoot to build new fission power plants in the United States. As of August 2008, there have been 17 approved new nuclear reactors with 8 more units to be approved by the end of the year [1]. It is timely to develop technology that could improve the safety, proliferation, and efficiency of new reactors. The mission of the Advanced Fuel Cycle Initiative (AFCI) is to "develop and demonstrate technologies that enable the transition to a stable, long-term, environmentally, economically, and politically acceptable advanced fuel cycle" [2]. In order to fulfill this mission, fuel separation procedures and Advanced Burner Reactor (ABR) technology need to be developed. In order for a burner reactor to 'eat' spent fuel from a pressurized water reactor (PWR) or a boiling water reactor (BWR), a high energy neutron spectrum (>0.1MeV), a high neutron flux ($\sim 8.0 \times 10^{15} \, cm^{-2} s^{-1}$), and a high operating temperature (>550C) is required [3]. The cladding of the fuel rods (pins) must withstand these extreme conditions for extended amounts of time. High Strength (HS) steels such as HT-9, ACO3, T91, and 316L are prone to stress corrosion cracking (SCC) and expansion/swelling from temperature and neutron flux gradients [4].

A promising cladding material for advanced fuel cycles is a metal matrix composite (MMC) in which ceramic fibers are bonded within a high-strength steel matrix, much like fiberglass. MMCs offer considerable benefit as a material for the nuclear fuel cladding tubes required for next-generation fission power reactors that must operate at extremely high temperature and high neutron flux. The tensile strength of some ceramic fibers is four to five times higher than HS steel so that a MMC is much stronger than its bulk metal counterpart. Therefore MMCs are a promising route for strengthening fuel cladding and thus lengthening the allowable exposure time and increasing the neutron flux. However, current MMC technology lacks the ability to effectively bond traditional high-temperature alloys to ceramic strands.

---

This thesis follows the style of the Journal of Applied Physics.

Ceramic strands (silicon carbide, boron nitride, or graphite) only bond well with aluminum, magnesium, or titanium. Aluminum and magnesium have too low of a melting point and Ti readily reacts with $O_2$ to create $Ti_2O_3$. None of these cases offer potential for cladding applications. Ceramics do not bond directly with HS steel [5].

In the design concept, a layer of Ti would first be applied [6]. Titanium reacts readily with the species on the fiber surface, producing excellent surficial bonding. It also has a temperature expansion coefficient that is intermediate between the (small) expansion of ceramic fibers and the (large) expansion of metals that might be desired in the matrix. A layer of the matrix metal would then be applied, so that the finished fiber has a surface that should bond readily to the desired matrix metal. The coated strand could then be integrated with the desired matrix metal to form the MMC in final-shape using any of several metallurgical techniques.
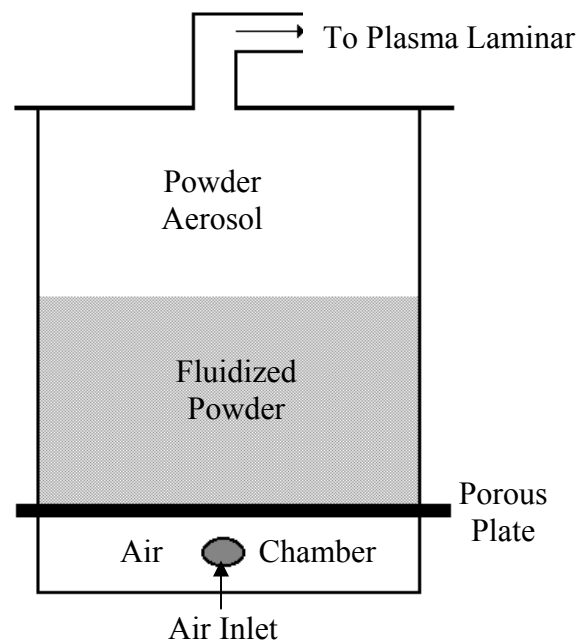


**Figure 1: Fluidizing Bed**

B. Background

The first piece of equipment in the conceptual design would be the Fluidizing Bed for creating the aerosols. Then the aerosols are heated through streamlines of a plasma torch and impinged upon a bare silicon carbide strand. The strand will need to be heated to ensure a good bond between the strand and the matrix metal [7]. This may potentially be done with the heat generated by the torch itself. The strand will be the precursor material for creating a MMC.

A schematic diagram for creating the metal aerosols is shown in Figure 1. The magnet lab at Texas A&M University has the capability of sorting particles to sizes less than 10 microns by means of a virtual impactor [8, 9]. Metal powders are readily available from several sources and creating aerosols from powders is not uncommon.
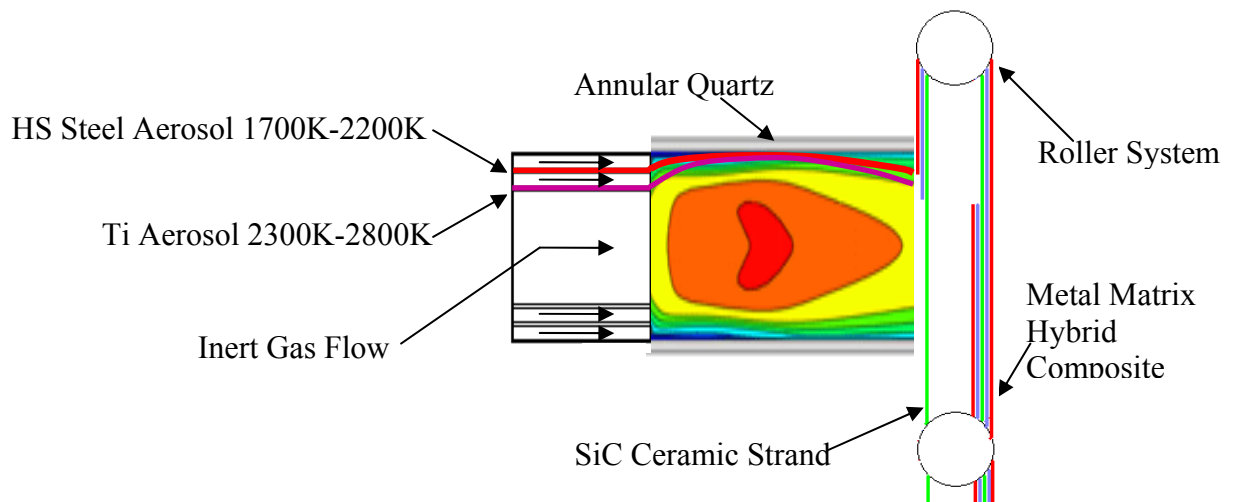


**Figure 2: Schematic Diagram of Torch System**

A schematic diagram for coating the SiC strands is shown in Figure 2. The aerosols created by the Fluidization System in Figure 1 will be introduced as labeled in Figure 2. The aerosol temperature will be rise according to the total integrated heat of

each laminar. The metal aerosol will then impinge upon the strands that have been heated from the roller system so that the silicon carbide would be completely, uniformly, and effectively coated with the matrix metal.

Perhaps the most crucial phase in this process is the characteristic temperature distribution and laminar flow of the plasma torch. If the two aerosols mix then we would destroy the effectiveness of the Ti adhesion layer. If the aerosols become too hot then they would evaporate. If the powder doesn't melt then the metals won't conform to the SiC surface. Without a well known temperature and velocity profile the concept will not work.

## C. Collaboration

The research at Texas A&M's Magnet Lab currently includes designing and building a plasma torch system and a fluidization bed for creating non-equilibrium phase reactions. Another motivation for developing the equipment is carbon-doping magnesium diboride ($MgB_2$), a type II superconductor. When carbon is introduced as a substitutional impurity in the $MgB_2$ lattice, it strains the lattice and thereby increases the upper critical magnetic field at which it remains superconducting.

## D. Conclusion

Using a plasma torch for producing a MMC has not been attempted before to the best of the writer's knowledge. If the project is successful in producing a robust and refractory nuclear fuel cladding, it might be possible to increase the longevity of a single fuel rod. This increase in core exposure time would enable a more complete burn for the fuel and decrease the required turnover for replacing fuel rods. The proposed materials technology would potentially assist in designing an ABR that could close the fuel cycle.

## II. MODELING PLASMA

### A. Plasma Modeling Introduction

Over the past 40 years plasma torch technology and interest has increased steadily. In the early seventies the bulk of the advancement was due to aerospace programs [10]. This increase was partly from a necessity to generate high temperatures to test reentry materials and for developing plasma propulsion systems. During the late seventies and early eighties there was a lull until 1984 when the number of thermal plasma technology patents tripled. This was caused by industry taking advantage of the seventies technology. Now using plasma torches and more specifically RF torches, has expanded in numerous applications. Some of the applications include powder spheroidization, plasma synthesis of ultra-fine nanostructure powder [11], and plasma deposition. Plasma deposition has several sub-categories including plasma sprays, plasma coatings for protection, and even plasma electrical circuitry deposition [12]. RF plasmas also treat waste materials by reclaiming useful material to recover added value and to deem hazardous materials as inert [10, 13]. All these process introduce the material into the exhaust plum of the plasma or on axis before the plasma. Our novel idea for using an RF plasma torch is to introduce the reactant directly into the plasma gas in the form of an aerosol.

The necessity of knowing the fluid dynamic flow and temperature profile of a plasma is critical to many applications. It's near impossible to build a plasma torch system to precise specifications without having working knowledge of the input parameter space or how each physical dimension effects flow. With time and money constraints it is not feasible to build an RF torch by trial and error. Therefore, accurate modeling ability is needed. Models for fluid dynamics, forces, and fields of an RF plasma have been done with increasing precision and accuracy in the past 30 years thanks to the advent of modern computing power. Modeling RF plasma began with theoretical dissertations and 1-D modeling [14-16] and has progressed to complete 3-D models [17, 18].

There are several Computational Fluid Dynamics (CFD) software packages available that can be altered to model plasma including a modified SIMPLER algorithm [19], SIMPLEC algorithm [20, 21], and the 2/E/FIX algorithm [22, 23] to name a few. In the past 15 years it seems the modeling software of choice has been a commercial computational fluid dynamics (CFD) software called FLUENT$^©$ [17, 24-26]. FLUENT$^©$ offers a magneto-hydrodynamics (MHD) add-on module for calculating coupled fields, forces, and heating [27]. However, a separate license must be obtained and the MHD module can be bypassed by means of using another feature of FLUENT$^©$. The platform by which FLUENT$^©$ was written enables one to write a User Defined Function (UDF) in c++ to add force and energy terms to the Navier-Stokes system of fluid dynamic equations. Additionally, one may also solve the field equations by means of initializing a User Defined Scalar (UDS) in FLUENT$^©$. With this in mind FLUENT$^©$ was chosen to model/design the plasma torch.

## B. Argon Plasma Assumptions

The study of the effects fields play on conductive fluids is called magnetohydrodynamics (MHD). On the ionic level the equations governing charge, velocity, and field are difficult to solve and are futile in the macroscopic scale. Therefore our model must look at plasmas in a statistical mechanical manner. The resulting differential equations, when all of the minor effects are added, are quite involved and difficult to solve except with numerical modeling. In order to model plasma effectively a few simplifications must be made and justified. The following assumptions are made for this model of plasma:

i.  The plasma is in Local Thermodynamic Equilibrium (LTE). This assumption allows us to define a unique temperature to each region of the plasma. LTE is invalid in regions of steep temperature gradients and for low pressure plasmas where the collision interactions are weak. With few collisions, individual particles can be accelerated by external forces to uncharacteristically fast velocities until the distribution is non-Maxwellian. Empirically, for pressures above 300 torr this is a safe approximation [28]. Above such pressures, the

concentration of particles is high enough so that they share energy through a high collision rate or small mean free pass.

ii. We assume that the plasma is azimuthally symmetric and the resulting fluid dynamic equations are two-dimensional ($\mathbf{B}_\theta, v_\theta = 0$).

iii. The coil impedance and self inductance and their effect on the power supply are collectively incorporated so that we can accurately set a known driving current in the coils.

iv. The induced current in the coils from the plasma is neglected.

v. We approximate the helixical shape of the copper pipe coils as 3 cylindrically symmetric, solid, and non-conducting rings. The non-conductivity property is a result of the previous 2 assumptions. This also ignores the axial component of coil current.

vi. The plasma gas is pure argon at atmospheric pressure.

vii. The plasma is modeled using a steady state time formulation.

viii. The plasma is modeled as entirely viscid (non-turbulent or laminar) with a Reynolds number not exceeding 1200 (this number comes from results). The accepted Reynolds number for macroscopic turbulent flow to begin in a circular cross section pipe is anywhere from 1800 to 2000 to 2300 [29-31].

ix. Viscous dissipation in the energy equation is neglected because the flow is mostly laminar.

x. Pressure work in the energy equation is dropped. The largest pressure increase is in the pre-plasma tube region and is less than a 0.2% gain. This would not significantly affect the total temperature of the plasma and can be safely neglected.

xi. The plasma is considered optically thin (OTP). This implies that the plasma doesn't absorb its own radiation. Therefore, a straight forward approach may be taken for temperature dependent radiation loss per unit volume.

xii. The displacement current term associated with an oscillating electric field is neglected in Maxwell's equations.

xiii. The plasma is quasi-neutral with no ambipolar diffusion contributions. In other words the number of ions and electrons are equal and they macroscopically move together.

xiv. In representing the entrainment between argon gas and plasma, we have assumed a smoothly-varying temperature dependence.

## C. Electromagnetic Field Theory

The high temperatures of an RF plasma come from the high field gradients driven by radio frequency currents in helixical coils. The coils and the plasma itself can be considered to be charge free if the power supply is grounded and the plasma has no ambipolar diffusion. With these initial conditions we write down Maxwell's equations that will govern the fields. In SI units we have:

$$\vec{\nabla} \bullet \vec{E} = \frac{\rho}{\varepsilon_0} \tag{1}$$

$$\vec{\nabla} \bullet \vec{B} = 0 \tag{2}$$

$$\vec{\nabla} \times \vec{E} = -\frac{\partial \vec{B}}{\partial t} \tag{3}$$

$$\vec{\nabla} \times \vec{B} = \mu_0 \varepsilon_0 \frac{\partial \vec{E}}{\partial t} + \mu_0 \vec{J} \cong \mu_0 \vec{J} \tag{4}$$

where $\vec{E}$ and $\vec{B}$ are the time dependent electric and magnetic field, $\vec{J}$ is the time dependent current density, $\mu_0$ is the permeability of free space, $\varepsilon_0$ is permittivity of free space, and $\rho$ is the electric charge density. The last equality from equation (4) follows from negligible displacement currents from the plasma conditions. This is a suitable approximation for phenomena where the characteristic velocities are much slower than the speed of light. As a proof we can see that Faraday's equation (3) gives us $E \sim Bl/t$ where $l$ and $t$ are a characteristic length (diameter of plasma) and time (inverse frequency) respectively [32]. Now if $v = l/t$ is the characteristic velocity of the fluid and $c\sqrt{\mu_0 \varepsilon_0} = 1$ is the speed of light in vacuum then the displacement current contribution goes like the following for 3MHz and $l \approx .05\,\mathrm{m}$:

$$\frac{\mu_0 \varepsilon_0 \left| \frac{\partial \vec{E}}{\partial t} \right|}{\left| \nabla \times \vec{B} \right|} \sim \frac{E/t}{c^2 B/l} \sim \left( \frac{v}{c} \right)^2 \sim 10^{-7} \, . \tag{5}$$

The contribution from the current is subsequently of order unity. Therefore any time variation of the electric field is too small to cause any high-velocity (on the order of the speed of light) charge distributions in the conducting plasma. So we can safely neglect the displacement current term.

From (2) and the vector calculus identity $\vec{\nabla} \cdot \left( \vec{\nabla} \times \vec{A} \right) = 0$, we may say that

$$\vec{B} = \vec{\nabla} \times \vec{A} \tag{6}$$

where $\vec{A}$ is the magnetic vector potential. Now the electric field has two sources. One contribution is from the charge density $\rho$ and the other from the varying magnetic field. We shall call them $\vec{E}_\rho$ and $\vec{E}_B$ respectively. Then from equation (3) and equation (6) we may say that

$$\vec{E} = \vec{E}_\rho + \vec{E}_B = -\frac{\partial \vec{A}}{\partial t} \, . \tag{7}$$

Then we have:

$$\nabla \cdot \vec{E}_\rho = \frac{\rho}{\varepsilon_0} \text{ and} \tag{8}$$

$$\nabla \times \vec{E}_B = -\frac{\partial \vec{B}}{\partial t} \, . \tag{9}$$

From conservation of charge we require that

$$\nabla \cdot \vec{J} = -\frac{\partial \rho}{\partial t} \tag{10}$$

which is the current continuity equation used to determine charge density in plasma.

Additionally, we may make use of another vector calculus identity:

$$\nabla \times \nabla \times \vec{A} = -\nabla^2 \vec{A} + \nabla \left( \nabla \cdot \vec{A} \right) \tag{11}$$

and after inserting equation (6) into (4) and invoking the Coulomb gauge $\left(\nabla \cdot \vec{A} = 0\right)$, we have:

$$-\nabla^2 \vec{A} = \mu_0 \vec{J} \tag{12}$$

where the last equality follows from (7).

Now to proceed, we need to make a simplification to the equations based on the properties of the plasma. At the highest frequency at which we can operate (5MHz) we have an electromagnetic wavelength of ~60meters. This characteristic length is 1000 times larger than the characteristic length of the plasma chamber. Therefore, the field can be approximately uniform over a macroscopic area so that a charge distribution could form. The mass of the electron is 80,000 times lighter than the plasma ions for argon. Therefore, the field gradients accelerate the electrons 80,000 times faster. However, as soon as the electrons move away from the ions, a localized field is created that slows the electrons and pulls the ions to comeback to charge and spatial equilibrium. We may describe a characteristic frequency by which the plasma would oscillate if in a field free region as:

$$\omega_p = \left(\sum_\sigma \frac{n_\sigma q_\sigma^2}{\varepsilon_0 m_\sigma}\right)^{\frac{1}{2}} \tag{13}$$

where the sum over $\sigma$ is over all of the different charge species [33]. Inserting numbers for argon at $10^4$ Kelvin at 1atm and using the ideal gas law we get:

$$\omega_p = \left(\sum_\sigma \frac{n_\sigma q_\sigma^2}{\varepsilon_0 m_\sigma}\right)^{\frac{1}{2}} = \left(\frac{n_p e^2}{\varepsilon_0 m_p} + \frac{n_e e^2}{\varepsilon_0 m_e}\right) = 4.8 \times 10^{13} \Big/ \mathrm{sec} \,. \tag{14}$$

This is much larger than the frequency at which the RF power supply operates at (3-5 MHz.). Therefore, the electrons and ions have ample time to come to equilibrium during each cycle. This equates to the plasma having no ambipolar diffusion contributions (from the different speeds of the electrons and ions).

Across the plasma there should not be any collections of charges so that the plasma obeys the quasi-neutrality property. These properties suppose that we may safely

state that the static charge distribution, $\rho$, is constant and zero. Therefore we may state the following:

$$\vec{\mathbf{E}}_{\rho} = \vec{0}. \tag{15}$$

Now we can assume an oscillatory solution with time dependence $\cos(\omega t + \varphi)$ where $\omega$ is the angular frequency of the RF generator, $t$ is time, and $\varphi$ is a location dependent phase shift. However, for simplification of calculation we use complex notation where the time dependence takes the form $e^{i(\omega t + \varphi)}$. With this time dependence we can simplify our system of equations so that (7) for example becomes:

$$\vec{\mathbf{E}} = -i\omega\vec{\mathbf{A}}. \tag{16}$$

With this simplification, we can also neglect the phase shift $\phi$ and absorb it by letting the vector potential and the fields be time independent and complex. Then we have:

$$\begin{aligned} \vec{\mathbf{A}} &= \vec{\mathbf{A}}_R + i\vec{\mathbf{A}}_I \\ \vec{\mathbf{E}} &= \vec{\mathbf{B}}_R + i\vec{\mathbf{B}}_I \\ \vec{\mathbf{E}} &= \vec{\mathbf{E}}_R + i\vec{\mathbf{E}}_I \end{aligned} \tag{17}$$

Now $\vec{\mathbf{J}}$ includes the current density from the RF power supply ($\vec{\mathbf{J}}_{coil}$) and from the induced currents in the plasma region and in the coils ($\vec{\mathbf{J}}_{ind}$) from plasma-coil coupling. The conductivity of the plasma is a function of temperature which we will write as $\sigma$. Conductivity is defined as the inverse of resistivity. With this definition we may write the current in the plasma region as:

$$\vec{\mathbf{J}} = \vec{\mathbf{J}}_{ind} = \sigma\vec{\mathbf{E}} = -i\omega\sigma\vec{\mathbf{A}}. \tag{18}$$

Likewise in the coil region we have

$$\vec{\mathbf{J}}_{coil} = \vec{\mathbf{J}}_{drive} + \vec{\mathbf{J}}_{coil \atop Self-induced} + \vec{\mathbf{J}}_{coil \atop Plasma-induced}. \tag{19}$$

In these equations, $\vec{\mathbf{J}}_{drive}$ is the current driven by the power supply voltage, $\vec{\mathbf{J}}_{coil \atop Self-induced}$ is the induced current from the coil self-induction, and $\vec{\mathbf{J}}_{coil \atop Plasma-induced}$ is the induced current from the mutual induction with the plasma.

We now invoke another assumption in modeling the plasma. To a first estimation the induced current in the coils and its effect on the plasma region is negligible. The validity of this statement is discussed and analyzed in appendix A. Theoretically, we must not neglect this contribution. Experimentally, we may simply adjust the power supply until the desired total current is reached. Therefore, for our modeling purposes, we will assume that we can accurately assign a total current to the coils. With this approximation the total current density in the coil region is:

$$\vec{\mathbf{J}} = \vec{\mathbf{J}}_{coil} = \frac{I_{coil}}{\pi a^2}\hat{\theta} \tag{20}$$

where $\mathbf{I}_{coil}$ is the current in the RF coils and $a$ is the coil radius. Here we assume that the current is evenly distributed in the coil. This method is chosen for its simplicity and ease of computations constraints in fluent. The coil is actually a hollow copper pipe with chilled, high-resistivity water flowing through. In the plasma region this small deviation should have zero to no effect upon the fields in the plasma region. The discrepancies will mostly arise near the coils and away from the plasma.

Also, for the magnetic scalar potential to have only one direction component, we are modeling the coils to be rings with cylindrical or azimuthal symmetry. This is probably the largest shortcoming in this model for plasma. However, for small angles of incline in the coils, this model should be accurate. In addition to the coil region, the current density in the walls and around the coils is zero because the conductivity of quartz and free space is miniscule.

*1. Magnetic Vector Potential Formulation*

Now recall that for a current distribution $\vec{\mathbf{J}}(\vec{r})$, we may evaluate the vector potential in cylindrical coordinates as:

$$\vec{\mathbf{A}}(\vec{r}) = \frac{\mu_0}{4\pi}\iiint \frac{\vec{\mathbf{J}}(\vec{r}')}{|\vec{r}-\vec{r}'|}d^3\vec{r}' = \frac{\mu_0}{4\pi}\iiint \frac{\frac{I_{coil}}{\pi r^2}\hat{\theta} - i\omega\sigma\vec{\mathbf{A}}(\vec{r}')}{|\vec{r}-\vec{r}'|}d^3\vec{r}' = (0, A_\theta, 0). \tag{21}$$

Here we have an integral equation where an iterative approach could be taken similar to the successive born approximations in quantum scattering theory. With (21), it is straight forward to see that the magnetic vector potential will only have $\hat{\theta}$ direction.

From (12), we may also write (21) as differential equation in cylindrical coordinates that can be programmed into FLUENT$^{©}$:

$$\frac{1}{r}\frac{\partial}{\partial r}\left(r\frac{\partial A_\theta}{\partial r}\right)+\frac{\partial^2 A_\theta}{\partial z^2}=\nabla^2 A_\theta=\left(\frac{A_\theta}{r^2}-i\mu_0\sigma\omega A_\theta-\frac{\mu_0 I_{coil}}{\pi a^2}\right)=-S_{A_\theta} \qquad (22)$$

or separating it into its real and imaginary parts:

$$\nabla^2 A_{R\theta}=\frac{A_{R\theta}}{r^2}-\mu_0\sigma\omega A_{I\theta}-\frac{\mu_0 I_{coil}}{\pi a^2}=-S_{A_{R\theta}}\text{ and} \qquad (23)$$

$$\nabla^2 A_{I\theta}=\frac{A_{I\theta}}{r^2}+\mu_0\sigma\omega A_{R\theta}=-S_{A_{I\theta}}. \qquad (24)$$

The $\frac{A_\theta}{r^2}$ terms arise from the Laplacian in equation (12) operating on a vector and not a scalar. See Table I for which source terms are included in each specific region.

In addition to solving the fluid dynamic governing equations, FLUENT$^{©}$ also has the capability to solve scalar potential equations like (23) and (24). The generalized scalar equation solved in FLUENT$^{©}$ is:

$$\frac{\partial \rho\phi_k}{\partial t}+\frac{\partial}{\partial x_i}\left(\rho u_i\phi_k-\Gamma_k\frac{\partial\phi_k}{\partial x_i}\right)=S_{\phi_k} \qquad k=1,\ldots,N. \qquad (25)$$

In this equation $\Gamma_k$ and $S_{\phi_k}$ are the diffusion coefficient and source term supplied by the user for each of the $N$ scalar equations. To adapt this equation to solve for the magnetic scalar potential we simply initialize the program to ignore convective mass flux $(\rho=0)$ and let the diffusion coefficient be unity. For the 2D axis-symmetric cylindrical coordinate case:

$$\frac{\partial}{\partial x_i}\left(\frac{\partial\phi_k}{\partial x_i}\right)=\nabla^2\phi_k=\frac{1}{r}\frac{\partial}{\partial r}\left(r\frac{\partial\phi_k}{\partial r}\right)+\frac{\partial^2\phi_k}{\partial z^2}=-S_{A_\theta}. \qquad (26)$$

With this equation, we define the source terms in each region as listed in Table I. With the terms programmed into FLUENT$^©$ via User Defined Functions, we are able to solve the magnetic scalar potential.

**Table I:** $A_\theta$ **Source Terms**

| Plasma Regions | Coil Regions | Wall Regions |
|---|---|---|
| $S_{A_{R\theta}} = \mu_0 \sigma \omega A_{I\theta} - \dfrac{A_{R\theta}}{r^2}$ | $S_{A_{R\theta}} = \dfrac{\mu_0 I_{coil}}{\pi a^2} - \dfrac{A_{R\theta}}{r^2}$ | $S_{A_{R\theta}} = -\dfrac{A_{R\theta}}{r^2}$ |
| $S_{A_{I\theta}} = -\mu_0 \sigma \omega A_{R\theta} - \dfrac{A_{I\theta}}{r^2}$ | $S_{A_{I\theta}} = -\dfrac{A_{I\theta}}{r^2}$ | $S_{A_{I\theta}} = -\dfrac{A_{I\theta}}{r^2}$ |

*2. Boundary Conditions*

Next, we must define boundary conditions for the scalar potential. For an extended field, approach far from the plasma region, it is most simple to implement vanishing boundary conditions for the vector potential, such that

$$A_\theta(\vec{r} = \vec{r}_{boundary}) = 0. \tag{27}$$

This is the equivalent to using the infinite boundary condition at the walls. This artificially increases the magnetic field values near the walls. A better and more sophisticated approach was constructed by Bernardi et al. by implementing dipole boundary conditions for $A_\theta$ [18]. This is equivalent to approximating the coil and plasma system as a single current loop at the center of the coils. The benefits from using this approximation will be analyzed with the results. We begin the progression with the vector potential for a current loop in the limiting case where the radius of the loop is much smaller than the observation point $(r^2 + z^2 \gg a^2)$ [34]. This formula also is valid for $r^2 + z^2 \ll a^2$.

$$A_\theta = \frac{\mu_0 I a^2}{4} \frac{r}{\left(a^2 + r^2 + z^2\right)^{3/2}} \tag{28}$$

In this equation, $r$ is the cylindrical coordinate. However, we don't know the value of the dipole vector for the plasma, namely $a$ or $I$. In other words, we don't know the contribution from the plasma region. We may bypass this requirement by setting the flux of $A_\theta$ through boundaries instead of setting the value. The flux through any boundary can be set by calculating the gradient dotted with the normal vector of the boundary:

$$\nabla A_\theta \bullet \hat{n} = A_\theta \left[ \left( \frac{1}{r} - \frac{3r}{r^2 + z^2} \right) \hat{r} - \frac{3z}{r^2 + z^2} \hat{z} \right] \bullet \hat{n}. \tag{29}$$

This equation assumes that the source is a dipole such that $a^2 \to 0$, $I \to \infty$, and $I a^2$ remains constant and is the dipole momentum magnitude. The gradient was taken in cylindrical coordinates. For each boundary, the normal vector should be directed outward of the calculated region to have the correct sign. The right hand side of equation (29) is what is programmed as the flux boundary condition for the vector potential in FLUENT©.

For this model, continuous boundary conditions for $A_\theta$ are used at material interfaces. From the cylindrical symmetry of the various quartz separation tubes we only have to be concerned with the tangential component of the electric field. Across any boundary with differing dielectric constants only the normal electric component is non-continuous:

$$\begin{aligned} \varepsilon_> \vec{E}_\perp \left( r_> \right) &= \varepsilon_< \vec{E}_\perp \left( r_< \right) \\ \vec{E}_\parallel \left( r_< \right) &= \vec{E}_\parallel \left( r_> \right) \end{aligned}. \tag{30}$$

Therefore, the electric field boundary condition is inherently obeyed. We also assume the magnetic permeability of all interfaces is continuous and equal in magnitude to the permeability of free space so that the components of magnetic field are continuous everywhere.

## 3. Field Calculation and Source Terms

From the real and imaginary parts of the magnetic scalar potential we are able to derive several source terms for the forces acting on the fluid and well as the resistive heating involved. From (6) and (16), we can write the complex electric and magnetic field components as the following:

$$E_\theta = -i\omega A_\theta \tag{31}$$

$$
\begin{aligned}
B_z &= \frac{1}{r}\frac{\partial}{\partial r}(rA_\theta)\\
B_r &= -\frac{\partial A_\theta}{\partial z}
\end{aligned}
\tag{32}
$$

The Lorentz force acting on the plasma would take the following form:

$$\frac{\vec{F}}{vol} = \frac{\overline{q\vec{v}\times\vec{B}}}{vol} = \frac{1}{2}\mathrm{Re}\left|\vec{J}\times\vec{B}^*\right| = \frac{\sigma}{2}\mathrm{Re}\left|E_\theta B_z^*\hat{r} - E_\theta B_r^*\hat{z}\right| = F_r\hat{r} + F_z\hat{z} \tag{33}$$

where the second equality comes from (18). The input format for source terms in FLUENT$^©$ is amount per volume. The leading ½ is an artifact of transferring from complex values of current and field to a real force. This arises from the time averaged value of $\overline{\left(e^{i(\omega t+\phi)}\right)^*\left(e^{i(\omega t+\phi)}\right)}=1$ being twice that of $\overline{\cos^2(\omega t+\phi)} = \frac{1}{2}$ which is the real component. In addition to the force we may also figure the power generated by the currents in the plasma. The resistive heating power or joule heating as coined in the literature is calculated as follows:

$$\frac{P}{vol} = \frac{\overline{VI}}{vol} = \frac{1}{2}\mathrm{Re}\left|\vec{E}\cdot\vec{J}^*\right| = \frac{\sigma}{2}\mathrm{Re}\left|\vec{E}\cdot\vec{E}^*\right| = \frac{\sigma}{2}\left|E_\theta\right|^2 = Q_{joule}. \tag{34}$$

## 4. Removal of Singularity

For the magnetic vector potential equation (22), the value of $A_\theta$ must approach zero faster than $r^2$ (2$^{nd}$ order pole) to prevent divergence. In order to have high precision of $A_\theta$ near the axis, FLUENT$^©$ must keep and store in memory very small numbers. This added uncertainty destabilizes the convergence of the code. The singularity can be removed by making a simple transformation:

$$A_\theta \mid A_\theta \Rightarrow rA'_\theta. \tag{35}$$

With this transformation (22) becomes:

$$\frac{1}{r}\frac{\partial}{\partial r}\left(r\frac{\partial A'_\theta}{\partial r}\right) + \frac{\partial^2 A'_\theta}{\partial z^2} = \nabla^2 A'_\theta = -\left(\frac{2}{r}\frac{\partial A'_\theta}{\partial r} + i\mu_0\sigma\omega A'_\theta + \frac{\mu_0 I_{coil}}{\pi a^2 r}\right). \tag{36}$$

Similarly this can be split into imaginary and real components similar to equations (23) and (24). From (36) we see that there is still a 1$^{st}$ order pole on the axis from the first term on the right hand side. However, azimuthal symmetry requires that the change in $A'_\theta$ in the radial direction must be zero on the axis. A similar argument could be made for $A_\theta$ on the axis but we can't show that it approaches zero faster than $r^2$. With the transformation, in each region we define the source terms in Table II. The difference in CPU time and convergence will be discussed with the results.

**Table II: $A'_\theta$ Source Terms**

| Plasma Regions | Coil Regions | Wall Regions |
|---|---|---|
| $S_{A_{R\theta}} = \mu_0\sigma\omega A_{I\theta} + \dfrac{2}{r}\dfrac{\partial A_{R\theta}}{\partial r}$ | $S_{A_{R\theta}} = \dfrac{\mu_0 I_{coil}}{\pi a^2 r} + \dfrac{2}{r}\dfrac{\partial A_{R\theta}}{\partial r}$ | $S_{A_{R\theta}} = \dfrac{2}{r}\dfrac{\partial A_{R\theta}}{\partial r}$ |
| $S_{A_{I\theta}} = -\mu_0\sigma\omega A_{R\theta} + \dfrac{2}{r}\dfrac{\partial A_{I\theta}}{\partial r}$ | $S_{A_{I\theta}} = \dfrac{2}{r}\dfrac{\partial A_{I\theta}}{\partial r}$ | $S_{A_{I\theta}} = \dfrac{2}{r}\dfrac{\partial A_{I\theta}}{\partial r}$ |

## 5. Fluid Dynamic Theory

The equations that are solved by FLUENT$^©$ are four-fold, coupled, linear, second-order, partial differential equations. The program allows us to input additional terms to the equations to give mass, force, and energy sources. The equations are in azimuthal cylindrical coordinates.

Mass Continuity Equation:

$$\frac{\partial \rho}{\partial t} + \frac{1}{r}\frac{\partial}{\partial r}(r\rho v_r) + \frac{\partial}{\partial z}(\rho v_z) = S_m \tag{37}$$

Momentum Conservation Equations:

$$\frac{\partial}{\partial t}(\rho v_z) + \frac{1}{r}\frac{\partial}{\partial z}(r\rho v_z v_z) + \frac{1}{r}\frac{\partial}{\partial r}(r\rho v_z v_r) = -\frac{\partial p}{\partial z} + \frac{1}{r}\frac{\partial}{\partial z}\left[r\mu\left(2\frac{\partial v_z}{\partial z} - \frac{2}{3}(\nabla\bullet\vec{v})\right)\right]$$
$$+ \frac{1}{r}\frac{\partial}{\partial r}\left[r\mu\left(\frac{\partial v_z}{\partial r} + \frac{\partial v_r}{\partial z}\right)\right] + F_z \tag{38}$$

$$\frac{\partial}{\partial t}(\rho v_r) + \frac{1}{r}\frac{\partial}{\partial z}(r\rho v_z v_r) + \frac{1}{r}\frac{\partial}{\partial r}(r\rho v_r v_r) = -\frac{\partial p}{\partial r} + \frac{1}{r}\frac{\partial}{\partial r}\left[r\mu\left(2\frac{\partial v_r}{\partial r} - \frac{2}{3}(\nabla\bullet\vec{v})\right)\right]$$
$$+ \frac{1}{r}\frac{\partial}{\partial z}\left[r\mu\left(\frac{\partial v_z}{\partial r} + \frac{\partial v_r}{\partial z}\right)\right] - 2\mu\frac{v_r}{r^2} + \frac{2\mu}{3r}(\nabla\bullet\vec{v}) + F_r \tag{39}$$

Where $\nabla\bullet\vec{v} = \dfrac{\partial v_z}{\partial z} + \dfrac{\partial v_r}{\partial r} + \dfrac{v_r}{r} = \dfrac{\partial v_z}{\partial z} + \dfrac{1}{r}\dfrac{\partial}{\partial r}(rv_r)$

Energy Conservation Equation:

$$\frac{\partial}{\partial t}(\rho H) + \nabla\bullet(\rho\vec{v}H) = \nabla\bullet\left(\frac{k_t}{C_p}\nabla H\right) + Q_{joule} - Q_{radiate} \tag{40}$$

For the preceding equations $\rho$ is the mass density, $v_r$ and $v_z$ is the radial and axial fluid velocity, $S_m$ is the mass source at the fluid inlet and outlet boundaries as defined by FLUENT$^©$, $\mu$ is the viscosity, $F_r$ and $F_z$ are defined by (33), $p$ is the static pressure, H is the enthalpy, $k_t$ is the thermal conductivity, $C_p$ is the specific heat capacity, $Q_{joule}$ is defined by (34), and finally $Q_{radiate}$ is the radiation energy lost. For these calculations, the material properties of $\rho$, $\mu$, $k_t$, and $C_p$ are all temperature dependent and calculated at a

constant pressure of 1 atmosphere. See appendix B for the material properties from the Sherbrooke group for argon from 300K to 13,200K [25]. The properties were modeled as piecewise continuous and not as a step function. However, Fluent doesn't let a user defined function be used to define the specific heat for a material. The latent heat of fusion and vaporization gives a Dirac delta discontinuity for this property and is difficult to model. Therefore, a special subroutine must be used in the program to account for latent heat and cannot be modeled with specific heat.

### D. Electromagnetic Field Theory in 3 Dimensions

To account for asymmetries in the coil and coil leads, we must ultimately develop a model to account for driving current in any direction. We begin with Maxwell's equations and keep the displacement current term:

$$\vec{\nabla} \cdot \vec{E} = \frac{\rho}{\varepsilon_0} \tag{41}$$

$$\vec{\nabla} \cdot \vec{B} = 0 \tag{42}$$

$$\vec{\nabla} \times \vec{E} = -\frac{\partial \vec{B}}{\partial t} \tag{43}$$

$$\vec{\nabla} \times \vec{B} = \mu_0 \varepsilon_0 \frac{\partial \vec{E}}{\partial t} + \mu_0 \vec{J} . \tag{44}$$

From (42) and the vector calculus identity $\vec{\nabla} \cdot \left( \vec{\nabla} \times \vec{A} \right) = 0$, we may again say that

$$\vec{B} = \vec{\nabla} \times \vec{A} \tag{45}$$

where $\vec{A}$ is the magnetic vector potential. Now the electric field has two sources. One contribution is from the charge density $\rho$ and the other from the varying magnetic field. We shall call them $\vec{E}_\rho$ and $\vec{E}_B$ respectively. Then we have:

$$\vec{\nabla} \cdot \vec{E}_\rho = \frac{\rho}{\varepsilon_0} = \vec{\nabla} \cdot \left( -\vec{\nabla} \phi \right) \tag{46}$$

from the static charge where $\phi$ is the usual electric scalar potential and

$$\nabla \times \vec{\mathbf{E}}_{\mathbf{B}} = -\frac{\partial \vec{\mathbf{B}}}{\partial t} \tag{47}$$

from the magnetic field. Or if we use equation (45) we have that

$$\vec{\mathbf{E}}_{\mathbf{B}} = -\frac{\partial \vec{\mathbf{A}}}{\partial t}. \tag{48}$$

Then combining equations (48) and (46) we have the following

$$\vec{\mathbf{E}} = -\vec{\nabla}\phi - \frac{\partial \vec{\mathbf{A}}}{\partial t} \tag{49}$$

for the total electric field. Additionally we may write the current density in the plasma region as the following:

$$\vec{\mathbf{J}} = \sigma \vec{\mathbf{E}}. \tag{50}$$

as an analog of Ohm's law. Now with a collection or distribution of charge, we can no longer assume ambipolar diffusion and the quasi neutrality property as assumed in the axis symmetric case. From conservation of charge we require that

$$\vec{\nabla} \bullet \vec{\mathbf{J}} = -\frac{\partial \rho}{\partial t} \tag{51}$$

which is the current continuity equation used to determine charge density in plasma. With this equation we may choose our gauge value for $\nabla \bullet \vec{\mathbf{A}}$. We begin with the traditional relation for figuring the vector potential:

$$\vec{\mathbf{A}}(\vec{r}) = \frac{\mu_0}{4\pi} \iiint \frac{\vec{\mathbf{J}}(\vec{r}')}{|\vec{r} - \vec{r}'|} d^3\vec{r}'. \tag{52}$$

Then taking the divergence with respect to the unprimed variable we have:

$$\vec{\nabla} \bullet \vec{\mathbf{A}}(\vec{r}) = \frac{\mu_0}{4\pi} \iiint \vec{\mathbf{J}}(\vec{r}') \bullet \vec{\nabla}\left(\frac{1}{|\vec{r} - \vec{r}'|}\right) d^3\vec{r}'. \tag{53}$$

Now using the following two identities for divergence:

$$\vec{\nabla}\left(\frac{1}{|\vec{r} - \vec{r}'|}\right) = -\vec{\nabla}'\left(\frac{1}{|\vec{r}' - \vec{r}|}\right) \quad \text{and}$$

$$\vec{\mathbf{J}}(\vec{r}') \bullet \vec{\nabla}'\left(\frac{1}{|\vec{r}' - \vec{r}|}\right) = \vec{\nabla}' \bullet \left(\frac{\vec{\mathbf{J}}(\vec{r}')}{|\vec{r}' - \vec{r}|}\right) - \left(\frac{\vec{\nabla}' \bullet \vec{\mathbf{J}}(\vec{r}')}{|\vec{r}' - \vec{r}|}\right) \tag{54}$$

we may transform equation (53) into the following:

$$\vec{\nabla}\bullet\mathbf{A}(\vec{r}) = -\frac{\mu_0}{4\pi}\iiint \vec{\nabla}'\bullet\left(\frac{\mathbf{J}(\vec{r}')}{|\vec{r}'-\vec{r}|}\right) - \left(\frac{\vec{\nabla}'\bullet\mathbf{J}(\vec{r}')}{|\vec{r}'-\vec{r}|}\right)d^3\vec{r}' = \frac{\mu_0}{4\pi}\iiint \frac{\vec{\nabla}'\bullet\mathbf{J}(\vec{r}')}{|\vec{r}'-\vec{r}|}d^3\vec{r}'. \quad (55)$$

The last equality follows from integrating the first term by parts. If the integration is over all space we assume the current density is zero at infinity so that the first term is dropped. Then using equation (51) we have the following:

$$\vec{\nabla}\bullet\mathbf{A}(\vec{r}) = -\frac{\mu_0}{4\pi}\frac{\partial}{\partial t}\iiint \frac{\rho(\vec{r}')}{|\vec{r}'-\vec{r}|}d^3\vec{r}' = -\mu_0\varepsilon_0\frac{\partial\phi}{\partial t} \quad (56)$$

where $\phi(\vec{r}) = \frac{1}{4\pi\varepsilon_0}\iiint \frac{\rho(\vec{r}')}{|\vec{r}-\vec{r}'|}d^3\vec{r}'$ is the usual integral for the electric scalar potential.

Now using vector identity (11) in equation (44) we have the following

$$\vec{\nabla}\times\mathbf{B} = -\nabla^2\vec{A} + \vec{\nabla}\left(\vec{\nabla}\bullet\vec{A}\right) = \mu_0\varepsilon_0\frac{\partial\vec{E}}{\partial t} + \mu_0\vec{J}. \quad (57)$$

If we use equation (49) for electric field and equation (56) for vector potential divergence we have the following vector equation to be solved:

$$\nabla^2\vec{A} = -\mu_0\vec{J} + \mu_0\varepsilon_0\frac{\partial^2\vec{A}}{\partial t^2} = -\mu_0\vec{J} - \mu_0\varepsilon_0\omega^2\vec{A} \quad (58)$$

where $\vec{J}$ is the coil current given by equation (20) on page 12 and the induced plasma current given by equation (50). For the plasma region this simplifies to:

$$\nabla^2\vec{A} = \mu_0\sigma\vec{\nabla}\phi + \left(i\omega\mu_0\sigma - \mu_0\varepsilon_0\omega^2\right)\vec{A}. \quad (59)$$

For the regions outside the plasma and the coils the value of $\vec{J}$ is set to zero in equation (58). These three dimensional equations may be programmed into FLUENT$^©$ following the same approach as equations (22) through (26) on page 13. It will be split into six different equations for the real and imaginary parts of the $x$, $y$, and $z$ components.

Now we must derive an equation for solving the scalar potential. From equation (41), we may simply plug in our electric field relation in the form of equation (49) and get the following result:

$$\nabla^2\phi = -\frac{\rho}{\varepsilon_0} + \mu_0\varepsilon_0\frac{\partial^2\phi}{\partial t^2} = -\frac{\rho}{\varepsilon_0} - \mu_0\varepsilon_0\omega^2\phi \tag{60}$$

which is very similar to the equation for vector potential. Equation (58) and (60) are commonly referred to as the MHD wave equations [35]. In this equation, we don't know what to use for the charge density as a function of position. However, we may find an expression for the charge density from the current continuity equation. Here we may write it using the phasor notation discussed with equation (16) on page 11 as the following:

$$\rho = \frac{i}{\omega}\vec{\nabla}\cdot\mathbf{J} \,. \tag{61}$$

Since we know that the only region that can collect charge is the plasma region, we may then write the current as $\sigma\vec{\mathbf{E}}$. When taking the divergence in equation (61) we must include the conductivity as a function of position so that

$$\vec{\nabla}\cdot\mathbf{J} = \sigma\vec{\nabla}\cdot\vec{\mathbf{E}} + \vec{\mathbf{E}}\cdot\vec{\nabla}\sigma \,. \tag{62}$$

Then with making use of relations (56) and (49) with some algebra we arrive at the following equation for the electric scalar potential:

$$\begin{aligned}\nabla^2\phi = -\mu_0\varepsilon_0\omega^2\phi &+ \frac{i}{\varepsilon_0^2\omega^2+\sigma^2}\Big[\varepsilon_0\omega\big(\vec{\nabla}\sigma\cdot\vec{\nabla}\phi\big) - \omega\sigma\big(\vec{\nabla}\sigma\cdot\vec{\mathbf{A}}\big)\Big]\\ &+ \frac{1}{\varepsilon_0^2\omega^2+\sigma^2}\Big[-\sigma\big(\vec{\nabla}\sigma\cdot\vec{\nabla}\phi\big) - \omega^2\varepsilon_0\big(\vec{\nabla}\sigma\cdot\vec{\mathbf{A}}\big)\Big]\end{aligned} \tag{63}$$

Outside the plasma region the conductivity is zero and thus the gradient is also zero. This equation will be split into a real and imaginary part just like the procedure in equations (22) through (26) on page 13.

Now the scalar potential has a dependence on the vector potential and the gradient of conductivity. In terms of solving this equation, a large conductivity gradient from a large temperature differential will result in divergent values for electric scalar potential. Therefore, in FLUENT© we will converge the data without the scalar potential contribution and then add in its effects to joule heating and forces.

*1. 3-D Singularities*

In three dimensions for Cartesian coordinates there is no need to transform variables to remove a singularity. This will enable us to use higher under-relaxation factors (see equation (74)) so that the six vector potential terms will converge with fewer iterations. However, there are 3 times as many equations to solve for the vector potential. Therefore, each iteration will take proportionately longer.

*2. 3-D Boundary Conditions*

Next, we must define boundary conditions for the vector and scalar potentials. For an extended field, approach far from the plasma region, it is most simple to implement vanishing boundary conditions, such that

$$\vec{A}(\vec{r} = \vec{r}_{boundary}) = 0$$
$$\phi(\vec{r} = \vec{r}_{boundary}) = 0 \qquad (64)$$

This is the equivalent to using the infinite boundary condition at the walls. This artificially increases the gradient near the walls. It is possible to implement dipole boundary conditions on the walls as given in equation (29). However, results from the two dimensional case show no visible contributions to the plasma temperature and flow patterns by using dipole boundary conditions. The electromagnetic field is altered only slightly along the walls. Therefore, the boundary conditions given in equation (64) will be used along the boundaries for the 3-D simulation.

For three dimensions, the electric boundary conditions for linear media are as follows:

$$\left( \varepsilon_1 \vec{E}_1 - \varepsilon_2 \vec{E}_2 \right) \cdot \hat{n} = \sigma \qquad (65)$$

$$\left( \vec{E}_1 - \vec{E}_2 \right) \times \hat{n} = 0 \qquad (66)$$

where $\sigma$ is the traditional symbol for sheet or surface electric charge and $\varepsilon$ is the material permittivity. In the axis symmetric case all of the material interfaces are parallel to the completely azimuthal electric field so that boundary conditions (65) are satisfied. If the current has an axial or radial component then theses boundary conditions become much

more complicated. The relative dielectric constant for quartz is somewhat low (3.8 to 5) so that the field lines shouldn't be greatly altered. Therefore, for this simulation, they will be bypassed by modeling the relative permittivity as unity.

The magnetic boundary conditions will have a larger effect and are as follows.

$$\left(\vec{\mathbf{B}}_1 - \vec{\mathbf{B}}_2\right)\bullet \hat{n} = 0 \tag{67}$$

$$\hat{n} \times \left(\frac{\vec{\mathbf{B}}_1}{\mu_1} - \frac{\vec{\mathbf{B}}_2}{\mu_2}\right) = \vec{\mathbf{K}} \tag{68}$$

where $\vec{\mathbf{K}}$ is the boundary sheet current and $\mu$ is the permeability of the material. The magnetic field is mostly axial and thus tangent to the material interfaces. Therefore, equation (68) will have a substantial effect on the field magnitude. The relative permeability of quartz (0.6) is less than unity so that field lines are pushed outside. The effects should be incorporated into the quartz wall boundary conditions for a more realistic model. However, most peer reviewed papers simply ignore theses magnetic boundary conditions [17-19, 24, 26]. For all subsequent simulations the inner wall boundary conditions should be included. To compare with other papers we also assume the magnetic permeability of all interfaces is continuous and equal in magnitude to the permeability of free space so that the components of magnetic field are continuous everywhere.

### 3. 3-D Field Calculation and Source Terms

From the real and imaginary parts of the electromagnetic scalar and vector potentials we are able to derive several source terms for the forces acting on the fluid and well as the resistive heating involved. The magnetic field is calculated from the curl of the vector potential and the electric field is calculated according to equation (49).

The Lorentz force acting on the plasma would take the following form:

$$\vec{\mathbf{F}} = \frac{\overline{q\vec{v} \times \vec{\mathbf{B}}}}{vol} = \frac{1}{2}\text{Re}\left|\vec{\mathbf{J}} \times \vec{\mathbf{B}}^*\right| = F_x \hat{x} + F_y \hat{y} + F_z \hat{z}. \tag{69}$$

The input format for source terms in FLUENT$^{©}$ is amount per volume. The leading ½ is an artifact of transferring from complex values of current and field to a real force as

discussed with equation (33). In addition to the force we may also figure the power generated by the currents in the plasma. The resistive heating power per volume or joule heating as coined in the literature is calculated as follows:

$$\frac{P}{vol} = \frac{\overline{VI}}{vol} = \frac{1}{2}\text{Re}\left|\vec{\mathbf{E}} \bullet \vec{\mathbf{J}}^*\right| = \frac{\sigma}{2}\text{Re}\left|\vec{\mathbf{E}} \bullet \vec{\mathbf{E}}^*\right| = \frac{\sigma}{2}\left|\vec{\mathbf{E}}\right|^2 = Q_{joule} \tag{70}$$

### 4. 3-D Fluid Dynamic Theory

The equations that are solved by FLUENT$^©$ are four-fold, coupled, linear, second-order, partial differential equations. The program allows us to input additional terms to the equations to give mass sources, add forces, and add energy. The equations are in azimuthal cylindrical coordinates.

Mass Continuity Equation:

$$\frac{\partial \rho}{\partial t} + \vec{\nabla} \bullet \left(\rho \vec{v}\right) = S_m \tag{71}$$

Momentum Conservation Equation:

$$\frac{\partial}{\partial t}\left(\rho \vec{v}\right) + \vec{\nabla} \bullet \left(\rho \vec{v}\vec{v}\right) = -\vec{\nabla}p + \vec{\nabla} \bullet \left[\mu\left(\vec{\nabla}\vec{v} + \vec{\nabla}\vec{v}^{\text{T}}\right) - \frac{2}{3}\left(\vec{\nabla} \bullet \vec{v}\right)I\right] + \vec{\mathbf{F}} \tag{72}$$

Energy Conservation Equation:

$$\frac{\partial}{\partial t}\left(\rho H\right) + \nabla \bullet \left(\rho \vec{v} H\right) = \nabla \bullet \left(\frac{k_t}{C_p}\nabla H\right) + Q_{joule} - Q_{radiate} \tag{73}$$

For the preceding three equations $\rho$ is the mass density, $\vec{v}$ is the fluid velocity, $S_m$ is the mass source at the fluid inlet and outlet boundaries as defined by FLUENT$^©$, $\mu$ is the viscosity, $\vec{\mathbf{F}}$ is defined by (72), $p$ is the static pressure, H is the enthalpy, $k_t$ is the thermal conductivity, $C_p$ is the specific heat capacity, $Q_{joule}$ is defined by (70), and finally $Q_{radiate}$ is the radiation energy lost. $\vec{\nabla}\vec{v}^{\text{T}}$ is the transpose of the vector gradient tensor $\vec{\nabla}\vec{v}$ and $I$ is

the 3 dimensional unit tensor. All property data for Argon is listed in appendix B. The gradient of conductivity term in equation (63) requires the first directional derivative be continuous. Therefore a quadratic interpolation formula was used between data points for conductivity. For all other variables a simple linear fit was used between data points.

## III. 2-D CODE VERIFICATION MODEL

To test the effectiveness and repeatability for our code and model we attempted to reproduce modeling results from the Plasma Technology Research Center at the University of Sherbrooke [25]. A company associated with this group called Tekna Plasma Systems Inc. has designed several induction plasma torches and the Tekna PL-50 was chosen for their model. Figure 3 shows the dimensions in millimeters of the plasma torch geometry.

In the top half, the dark green regions are coils and the light green regions are quartz walls. The gray regions will be fluid flow modeling and the light gray region is where the plasma source terms will be implemented. The outer region is needed for manipulating FLUENT$^©$ to calculate the electromagnetic fields. The flow rates and the frequency are listed in Table III.

The bottom half of Figure 3 is the grid produced in GAMBIT$^©$ which is a preprocessor program for FLUENT$^©$ [36]. In the plasma, fluid flow, and quartz tube we have a structured triangular grid with roughly 9 cells per square millimeter for 49,616 total cells. In the coils and extended field region we have an unstructured triangular grid with 53,382 total cells. The Sherbrooke model has $54 \times 80 = 4320$ quadrilateral cells in the fluid/quartz region and 7489 unstructured triangular cells in the extended field region. Having more cells for our model will help with convergence but will cost extra CPU time. A smaller grid size was chosen because of a small difference in grid.

The Sherbrooke model does not include the Q3 flow pipe and quartz tube (from $y = 0$ to 3.7 and $x = 0$ to 50 in Figure 3). This region has a small characteristic length that allows a larger grid size to be used effectively if removed. The author elected to compare the different Q3 region models and thus has a larger number of cells in the plasma region.
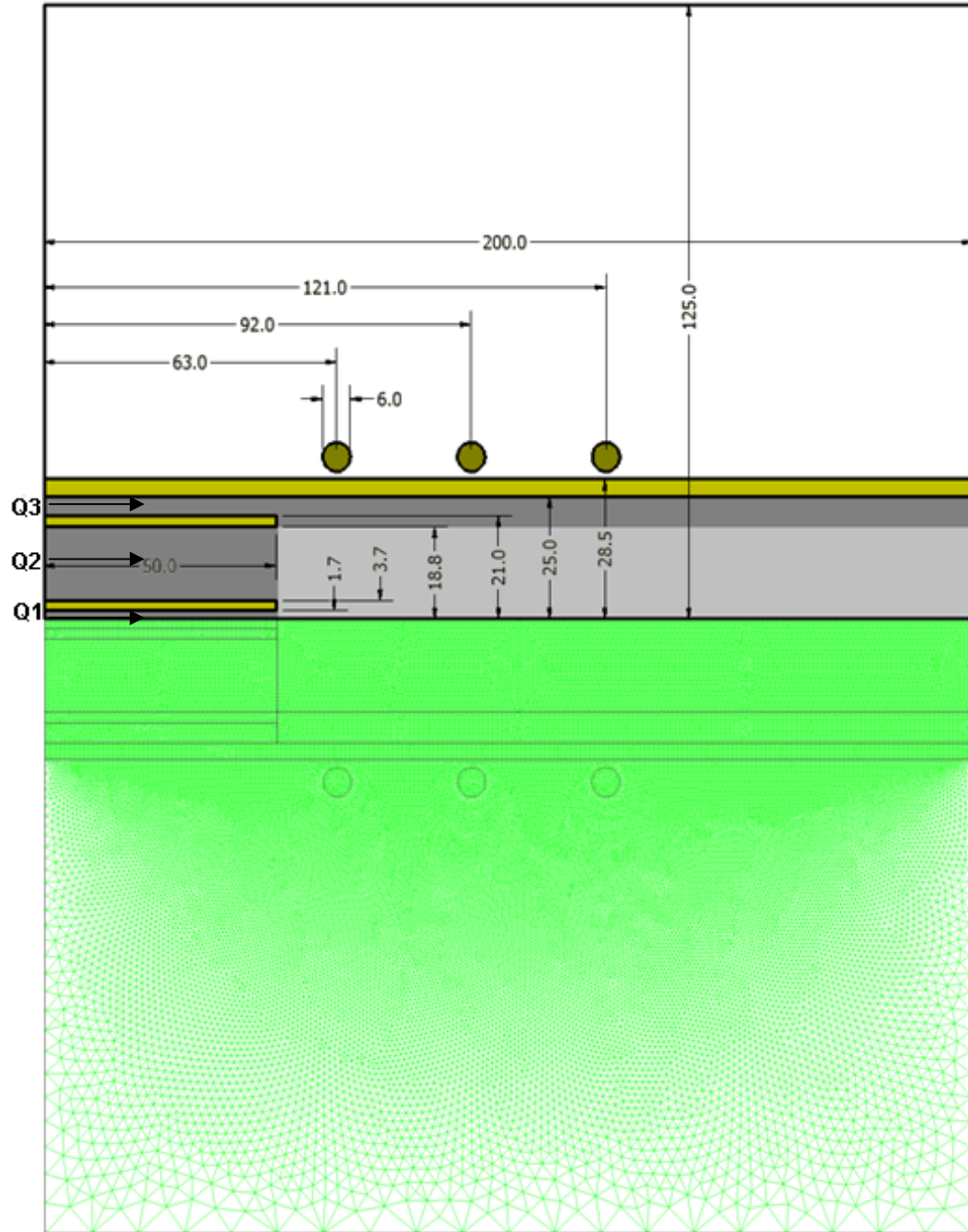
**Figure 3: Tekna PL-50 and Gambit Grid**

**Table III: Argon Plasma Input Data**

| Q1 | Q2 | Q3 | Frequency |
|---|---|---|---|
| 1slpm = 1.8357m/s | 3slpm = 0.0468m/s | 31slpm = 0.8938m/s | 3MHz |

For Table III, the equivalent speed of argon through the corresponding geometric cross sections is converted from slpm (standard liters per minute) which is the format of the Sherbrooke model. The frequency of oscillation for the torch is 3MHz which implies the angular frequency is $1.885 \times 10^7$ radians per second. The maximum coil current is 161 Amps.

## A. Methods of Code Convergence

There are a few key elements that need special attention in order for the model to iterate and converge on the desired result. This includes correctly defining model schemes, setting effective control parameters, and finding efficient initial values and conditions for the field and fluid properties.

### 1. Computer Licensing

Two licensed supercomputers were used at Texas A&M for Fluent$^©$ and Gambit$^©$ software programs. Another single-user license for Vector Fields$^©$ was used on a desktop machine at TAMU Magnet Laboratory for electromagnetic field verification.

The first supercomputer is a 32 processor IBM Regatta p690 called Agave. It is powered by IBM POWER4 processors that operate at 1.3GHz. The memory size is 64GB. The cumulative CPU time was roughly 20 hours.

The second supercomputer named Hydra, is a 640-processor IBM Cluster system with 1.9HGz power5+ processors. The processors are split into nodes of 16 processors and 32GB of memory. The total CPU time was over 30 hours.

*2. Model Schemes and Control Parameters*

FLUENT$^©$ is a very powerful computational fluid dynamics (CFD) program that includes schemes for modeling compressible flows, turbulent flows, supersonic flows, heat and mass transfer, reactionary and multiphase flows, and everywhere in between. As stated with the assumptions, we will be modeling laminar, axis-symmetric, 2 dimensional flow. The pressure based solver will be used because it has the best convergence for low-speed incompressible flow. Similarly, within the pressure based solver we will use the coupled approach that solves the momentum and continuity equations simultaneously rather than sequentially. This takes more memory, but the coupled solver converges quicker [37]. The iterative process that was taken to model the plasma can be depicted by Figure 4.

The parallelograms and hexagons in Figure 4 are the respective input parameters and source terms for each step of the iteration. The sequence begins with iterating the vector potentials. The results from this first step are used as force source terms for iterating the fluid dynamic equations. The mass flux is calculated using the inlet boundary conditions Q1, Q2, and Q3 as source terms and iterating the mass continuity equation. The last equation before testing convergence is the energy or temperature equation. For a discussion of each UDF source term see appendix C.

Each of the four fluid dynamic equations and the two vector potential equations can be exactly solved for the boundary conditions of each cell. This would include solving a system of over 600,000 equations and unknowns for the test model. The impracticality of solving such a system requires another method be used. Fluent works by method of finite difference. An initial value is chosen for each cell and for each variable (temperature, $A_{R\theta}, A_{I\theta}, v_z, v_r$, and pressure). Then for each iteration, the program updates the cell variables based on the values of neighboring cell values and obeying the governing equation.
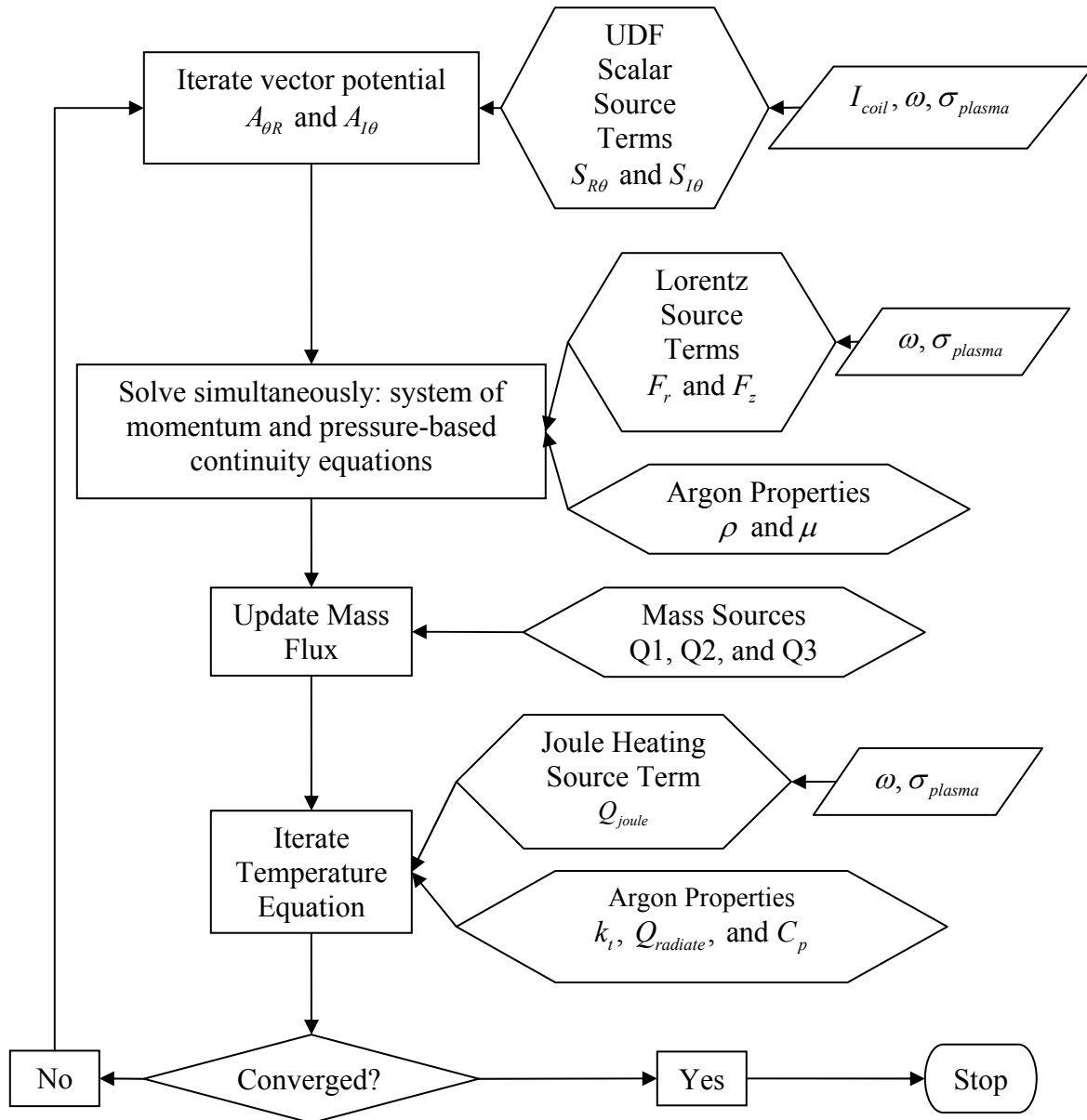
**Figure 4: Flow Chart for the Coupled Pressure-Based Solver**

A second-order upwind scheme was used for the test model that takes into account each neighboring cell and their neighbors. This scheme takes longer to converge and is slightly more unstable as opposed to a first-order scheme. However, it produces a more realistic and continuous fluid flow representation. From the non-linearity of the equation set being solved it is necessary to control the change of each variable for each iteration.

If $\phi$ is the variable in question and $\nabla\phi$ is the amount of variable change to satisfy the instantaneous conditions then the updated value would be written as the following:

$$\phi_{new} = \phi_{old} + \alpha\nabla\phi \tag{74}$$

where $\alpha$ is called the under-relaxation factor. There are similar factors that control the coupling between the continuity equation and the momentum equations. By much tweaking, trial, and error, Table IV lists the under-relaxation factors and acceptable ranges for the test model. The pressure and momentum factors have to do with the coupling between mass and momentum. The density factor deals with updating momentum and density. The listed labels for vector potential use the same notation as in equation (35). Fluent suggests starting each under-relaxation factor anywhere between 0.90 and unity. However, the strong coupling between Lorentz forces, Joule heating, and the vector potential gives a large numerical instability for convergence. Therefore each factor was greatly reduced.

**Table IV: Under-Relaxation Factors**

| Variable | Density | Pressure | Forces | Energy | Momentum | $A_\theta$ | $A_\theta'$ |
|---|---|---|---|---|---|---|---|
| Relax factor $\alpha$ | .35 | .75 | .35 | .35 | .75 | .60 | .80 |
| Relax range | .15-.45 | .50-.80 | .15-.45 | .10-.45 | .50-.80 | .50-.60 | .65-.80 |

*3. Convergence*

There are several steps in initialization and patching during the early iterations that were done in assisting convergence. The initial value for velocity was 0.5m/s in the axial direction and 0.0m/s in the radial direction in the fluid regions. The Sherbrooke group modeled the outside region as a fluid. To keep the flow at zero, they added source terms via UDF to keep the velocities zero and temperatures at 300K. For the test run, we are modeling the outside region as a solid. This saves precious computational time by removing the Navier-Stokes equations for the outside region and will give the same computational result in the plasma region. However, to keep the temperature near 300K in the outside region we added an artificial energy source term in the form of the following:

$$S_{outside} = -10^5 (T - 300K) \frac{W}{m^3}.$$  (75)

The vector potential was initialized to zero everywhere. The temperature was set to 300K everywhere except inside the plasma region where the temperature was set to 9000K.

The high initial temperature in the plasma region gave a large discontinuity initially and thus all the under-relaxation factors (except $A_\theta$ and $A_\theta'$) had to be decreased to the low end of their range to prevent divergent iterations. However, a high temperature in the plasma region is required to initialize the imaginary component of the vector potential. The high temperature gives high electric conductivity to the plasma region. The conductivity of plasma is proportional to the only imaginary current source term. Therefore, with a high initial temperature the imaginary component of the vector potential would have a substantial initial source term value. For the first 1000 iterations an artificial source term was used in the plasma region of the form:

$$S_{Plasma,\,Temporary} = -10^4 (T - 9800K) \frac{W}{m^3}.$$  (76)

This also allowed the magnetic field magnitude to increase so that resistive heating could sustain the plasma.

Initially the current in the coils was modeled at 250 amps. This over estimation for current in the coils allowed the vector potential to sustain plasma quicker because of higher fields and greater joule heating. Once the plasma was self-sustaining, the current was reduced to the given value of 161 amps.

## *4. Singularity Removal*

As previously revealed with equations (35) and (36), the transformation rids ourselves with having a diverging 2$^{nd}$ order pole vector potential source term on the axis. However, the transformation gives us a pesky gradient term with each source term as revealed in the tables on pages 14 and 17.

Two different UDF c++ codes were written for $A_\theta$ and $A'_\theta$. Both codes were used for the test model with identical results for temperature, field, and flow. The only difference is in convergence and speed. The code for using $A_\theta$ iterated 5% faster than the UDF for $A'_\theta$. I believe that for $A'_\theta$, the increased iteration time is from the source terms having both vector potential and gradient terms i.e. $A_\theta$ and $\vec{\nabla} A_\theta$. The UDF source terms for $A_\theta$ only includes the vector potential. However, the difference in iteration time between the two forms is relatively small at a part in twenty.

The benefit from removing the singularity outweighs the increased length of each iteration. With the singularity removed, the numerical stability of FLUENT$^©$'s scalar potential solver is increased. In Table IV, we see the effects of this stability in that the maximum under-relaxation factor for $A'_\theta$ is 0.2 higher than $A_\theta$. This implies that with each iteration, the $A'_\theta$ UDF is able to converge 20% more than $A_\theta$. In the simplest case for one cell, if $\alpha$ is the under-relaxation constant, $N$ is the number of iterations and $R = 10^{-6}$ is the residue then the governing equation for the amount of required iteration would be the following:

$$(1-\alpha)^N = R \quad \Rightarrow \alpha = .6, N = 16 \atop \Rightarrow \alpha = .8, N = 9 \quad . \tag{77}$$

The small change in under-relaxation factor changes the number of required iterations drastically. In multi-cellular cases the same ratio generally holds. For example, for 200 Amps with the test model, it took ~8,000 iterations to converge with a residue from $10^{-5}$ to $10^{-6}$ for $A'_\theta$. It took ~14,500 iterations to converge the same amount for $A_\theta$. Therefore, with each subsequent model, the $A'_\theta$ user defined function code will be used for stability and speed of convergence. However, to diminish confusion the $A_\theta$ notation will be used.

## 5. Judging Convergence

The FLUENT$^©$ definition of Residue can be defined as a quantitative amount that the cell values violate the governing differential equations. After discretization into cells, the conservation equation for a general variable $\phi$ at cell $P$ is as follows:

$$a_P \phi_P = \sum_{nb} a_{nb} \phi_{nb} + b \tag{78}$$

where $a_P$ is the center coefficient, $a_{nb}$ is the influence coefficients for neighboring cells, and b is a constant that represents sources. From this equation we may write the scaled residuals $R_\phi$ as the following:

$$R_\phi = \frac{\sum\limits_{\text{all cells } P} \left| \sum\limits_{nb} a_{nb} \phi_{nb} + b - a_P \phi_P \right|}{\sum\limits_{\text{all cells } P} a_P \phi_P} . \tag{79}$$

From this equation, we see that the residue represents the ratio of variable error to variable value. FLUENT$^©$ recommends that residue values be at most $10^{-3}$ for flow variables and $10^{-6}$ for energy. Table V gives the residues for the test model.

**Table V: Test Model Residues**

| Mass Continuity | Axial Momentum | Radial Momentum | Energy | $A_{R\theta}$ | $A_{I\theta}$ |
|---|---|---|---|---|---|
| $1.5\times10^{-6}$ | $2\times10^{-11}$ | $1\times10^{-11}$ | $9\times10^{-11}$ | $4.5\times10^{-14}$ | $3.2\times10^{-13}$ |

The flow variable residues were converged after 40,000 iterations and the field variable residues, $A_{R\theta}$ and $A_{I\theta}$, continued to decrease until 90,000 iterations. As an example of residue verification we may sum the mass flux at the inlet and outlet. The difference between the inlet and outlet mass flux for the test model was $2.49 \times 10^{-12}$ kg/s with the mass flow being $9.47 * 10^{-4}$ kg/s. This would produce an estimate for the mass continuity residue of $R_\phi^{Mass} = \dfrac{2.49 \times 10^{-12}}{9.47 \times 10^{-4}} = 2.63 \times 10^{-9}$. However, the absolute value in equation (79) assures that this value is an absolute minimum for the mass residue. None the less, the residues given in Table V should be more than adequate for verifying the convergence of the code.

## B. Results

### 1. Temperature Discussion

Figure 5, Figure 6, and Figure 7 give plasma results from the Sherbrooke model. The temperature distribution in Figure 5 and the temperature distribution on page 38 appear to be very similar. The maximum temperature for the Sherbrooke and 2-D model was 9920K and 10002K respectively. The horizontal scale is increased by a doubling factor in all flow figures to see the features and match the figures of the Sherbrooke group. The maximum value for joule heating was $1.41 \times 10^8$ W/m3 for the Sherbrooke model in Figure 7 and $1.55 \times 10^8$ W/m3 for the 2-D test model on page 38.

The maximum temperatures coincide with less than a percent difference and the contour lines have the same shape. There are approximately 500 cells of the $4.3 \times 10^4$ fluid cells that have temperatures over 9900K in the test model. With the given mesh sizes, the Sherbrooke model would have 41 cells in the same region. Over 9950K, there would be only about 3 Sherbrooke cells in comparison to 40 cells in the test model. For Joule Heating, there are roughly 40 test model cells for amounts over $1.4 \times 10^8$ Watts/m$^3$ in comparison to only 3 for the Sherbrooke model. Cell variables are an average or an estimate over the volume or area of a cell. This could potentially explain why the mesh

size has such an effect over the maximum temperature and maximum joule heating for a set driving current.

The two visual discrepancies seem to arise at the wall between the Q2 and Q3 regions and the Q1 outlet. At the wall between Q2 and Q3, the test model seems to have conducted heat further toward the inlet than the Sherbrooke model. This can be explained by the test model using a different thermal conductivity and specific heat for the wall material compared to the Sherbrooke model. However, both models are modeling quartz for a wall material.
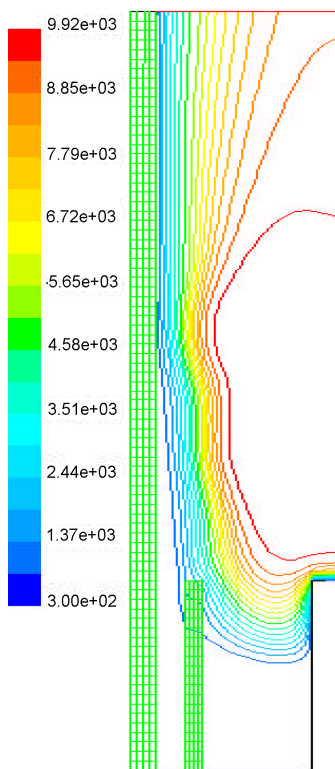


**Figure 5: Sherbrooke Temperature (K)**
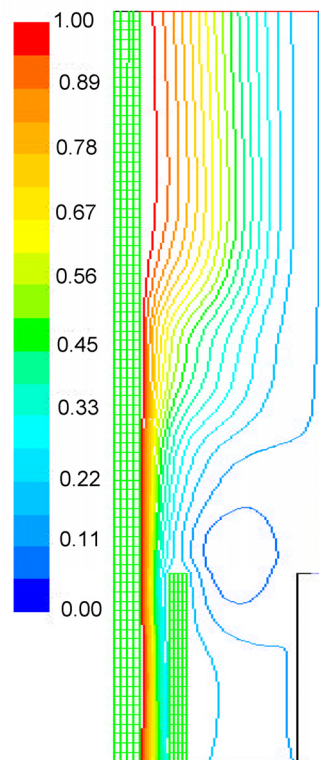
**Figure 6: Sherbrooke Stream Function (kg/s)**
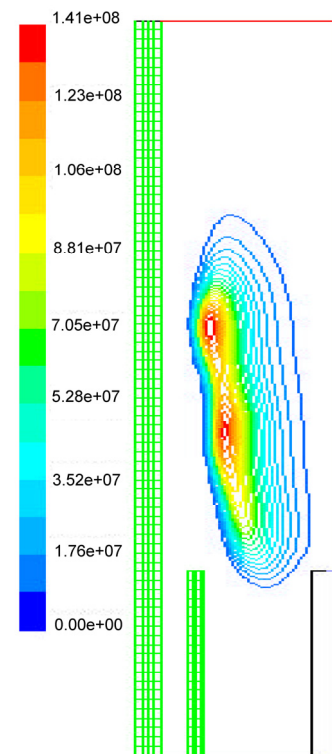
**Figure 7: Sherbrooke Joule Heating $W/m^3$**

Both models are modeling quartz for a wall material. The thermal conductivity of quartz is less than $1/100^{th}$ of most metals and twice that of argon at $10^4$K. Therefore, the number of time-steps and/or iterations required for heat transport is increased compared to argon. Thus, the difference can be explained by several more iterations for the test model compared to the Sherbrooke model.
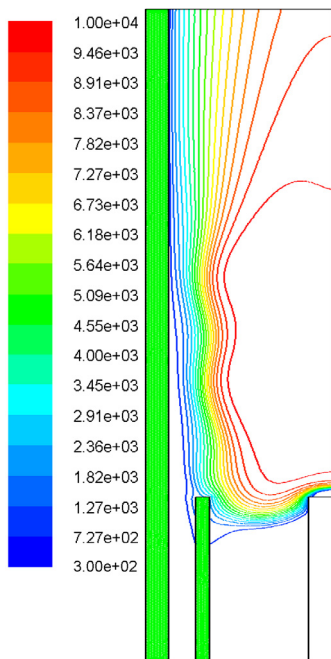


**Figure 8: 2-D Model Temperature (K)**
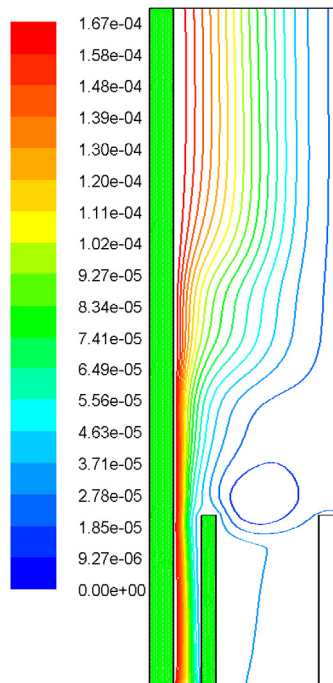
**Figure 9: 2-D Model Stream Function kg/s**
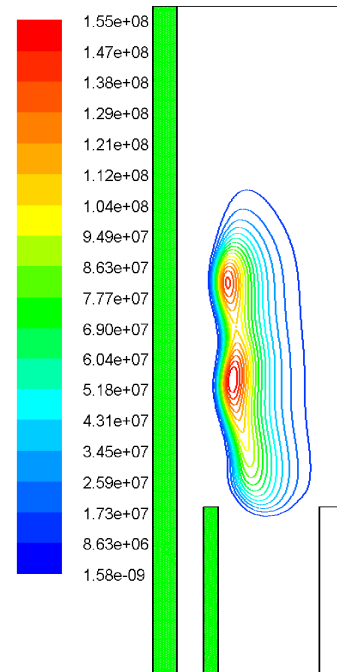
**Figure 10: 2-D Model Joule Heating** $W/m^3$

At the Q1 outlet, the test model has a region where the temperature remains 300K and the Sherbrooke model has the temperature immediately increasing. This corresponds to plasma being present at the Q1 interface for the Sherbrooke model and plasma beginning at some distance (~3mm) away for the test model. Argon is non-

conductive at 300K and thus there should be no joule heating. The gas must be mixed or convectively heated to roughly 4000K for joule heating to be significant. For convection, the energy needed to heat the Q1 inlet gas to 4000K in 1 second is $\int C_p \cdot V \cdot \Delta T \approx 62.8$ Joules. The maximum heat transferred by conduction for 1 second is $k \cdot A \cdot \dfrac{\Delta T}{x} \approx .002$ Joules, where $k$ is the thermal conductivity, $A$ is the surface area, and $x$ is the conduction length. Therefore, the argon at inlet Q1 is not heated by conduction but is heated by mixing or convection. The test model was able to render a laminar flow region near Q1 and a mixing region about 3 millimeters from the inlet. With a larger cell size, the Sherbrooke model doesn't predict this region but showed the mixing region immediately at the inlet. This effect is also seen in how the stream functions differ.

## *2. Stream Function Discussion*

Figure 8, Figure 9, and Figure 10 give plasma results from the 2-D Test Model. The Stream Function is an isocontour of the total amount of gas flowing in kg/s from the center of the inlet to a radial distance. Figure 6 and the stream figure on page 38 both have 18 streamlines and have similar shape. However, the Sherbrooke model doesn't render any streamlines from Q1. This may be from the location of the mixing region as discussed previously. However, this is unlikely because of what the location of the origin of each line of the Stream Function in FLUENT[©] represents. The Stream Function is formulated to combine information about the streamline flow of argon and conservation of mass. Each line represents a certain amount of argon at the inlet.

The differences in the starting locations of each line implies either a different initial velocity condition or a difference in the GAMBIT[©] mesh or grid. A difference in initial velocity is viable through confusion in what the boundary condition should be at Q1, Q2, and Q3. Most meters measure volumetric flow. Therefore, using a set velocity over a cross sectional area is the most reproducible boundary condition.

The Sherbrooke paper doesn't specify what type of inlet is used whether constant mass or constant velocity. However, from a personal communication with Siwen

Xue [38], we know the Sherbrooke model used constant mass. This test model along with a similar model by a group from Bologna, Italy [39] uses a constant velocity as the inlet boundary condition. Using slpm units implies constant volume and thus velocity. However, often using standard units implies constant mass at a standard temperature of 293.15K and standard pressure of 1 atmosphere. From the ideal gas law we know that if volume and temperature is constant and pressure changes then the mass flow rate changes. This corresponds to the constant velocity case. We also know that if the mass flow rate and temperature is constant and pressure changes, then the velocity must change. This corresponds to the constant mass case. The two cases would be identical if the inlet temperature was at STP, but the models use 300K. Even then, the Stream Function would simply be scaled differently, but the origin of each streamline would be in the same location. In other words, because Q1, Q2, and Q3 is in the ratio 1, 3, 31 slpm respectively the starting location of each streamline should be in the same location regardless of constant mass or volume as the boundary condition. This follows from modeling the flow as incompressible. A compressible flow would not require the boundary conditions to be identical. The converged result with constant mass flow boundary condition gives identical results with. Therefore, this explanation is incorrect.

The most likely explanation of the different starting locations for the streamlines is from the mesh sizing. A smaller cell size along the inlet boundary would allow the Stream Function to evenly disperse the streamlines. Thus, from the different cell sizes and dispersions the starting locations for the streamlines are not identical.

### 3. Vector Potential Discussion

The extrema for the Sherbrooke model vector potential was $1.07\times10^{-4}$ T m and $-5.87\times10^{-7}$ T m for the real component and $-1.44\times10^{-5}$ T m for the imaginary component in Figure 11 and Figure 12. The 2-D Test model had $1.101\times10^{-4}$ T m and $-3.494\times10^{-6}$ T m for the real and $-1.477\times10^{-5}$ T m for the imaginary in Figure 13 and Figure 14.
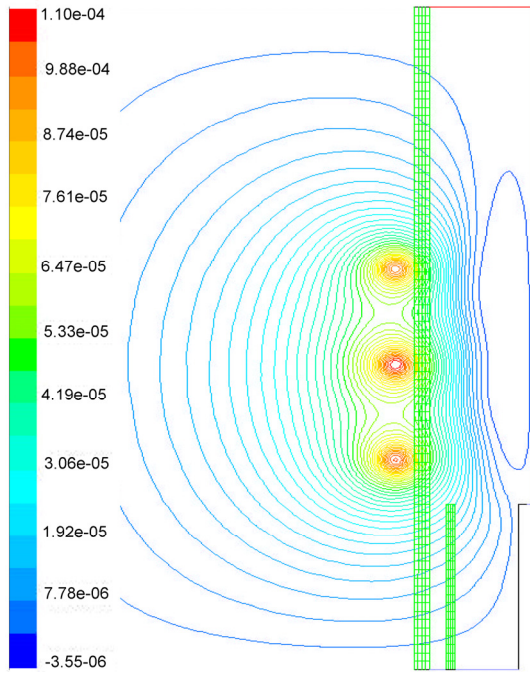
**Figure 11: Sherbrooke Model** $A_{R\theta}$
**(T m)**
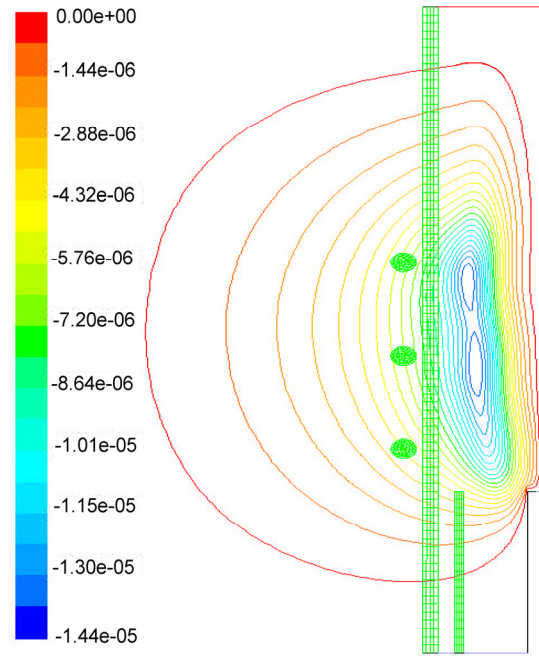


**Figure 12: Sherbrooke Model** $A_{I\theta}$
**(T m)**

For both the Sherbrooke and the test models, the boundary value of $A_\theta$ at all walls is set to zero. Setting the potential to zero along the boundary is artificial to a small extent. The largest effect will be seen closest to the coils. This boundary condition is applied at the Q1 boundary and therefore the largest deviation from reality should be at this boundary. Further analysis will be conducted with dipole boundary conditions.

There is slight difference between the two vector potentials in extrema values. The test model value for max $A_{\theta R}$ has a 3% higher value than the Sherbrooke model. The test model value for max $A_{\theta I}$ has a 2% larger absolute value than the Sherbrooke model.

**Figure 13: 2-D Test Model $A_{R\theta}$ (T m)**
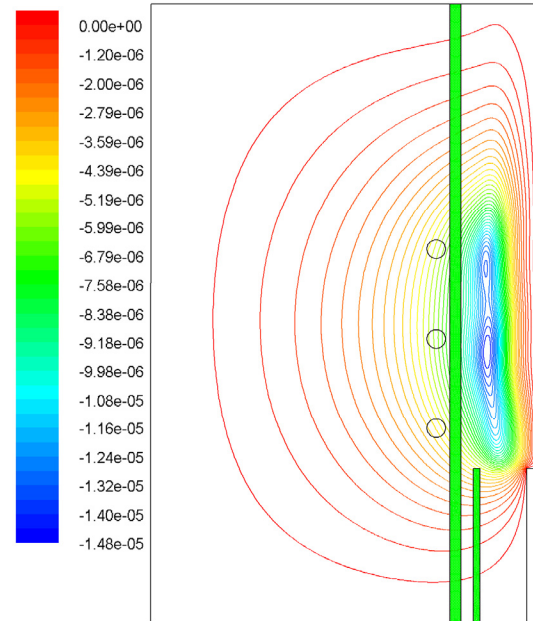


**Figure 14: 2-D Test Model $A_{I\theta}$ (T m)**

Both the real and imaginary parts of the magnetic vector potential appear to be replicated between the Sherbrooke model and the test model. The real components have a negative value in the center of the plasma. This is expected because the magnetic field is completely shielded in the center of the plasma. More so, the field is in the opposite direction in the center of the plasma from the induced currents. However, there is slight difference between the two in extrema values. The test model value for $\max A_{\theta R}$ has a 3% higher value than the Sherbrooke model. Additionally, test model value for $\max A_{\theta I}$ has a 2% larger absolute value than the Sherbrooke model.

Joule heating is the direct cause for having a 1% higher maximum model temperature. The indirect cause could be from having a slightly different flow pattern near the Q1 inlet. This would be consistent with the temperature discussion of the mixing region near the Q1 inlet. Different flow patterns change the localized temperature which effects conductivity. The conductivity drives the vector potential. The magnitude

of the effects from the Q1 region will be much more visible by extending the modeling field in the dipole boundary condition (DPBC) model.

### C. Dipole Boundary Condition (DPBC) Model

In the DPBC model, we have extended the flow field to include the pipe and wall carrying the central Q1 flow. We have also have defined magnetic dipole boundary conditions with the dipole momentum along the axis and located in the center of the middle current coil. The extrema for the real component of vector potential was $1.105 \times 10^{-4}$ T m and $-3.678 \times 10^{-6}$ T m in Figure 15. The minimum value for the imaginary was $-1.561 \times 10^{-5}$ T m for the DPBC model in Figure 16.
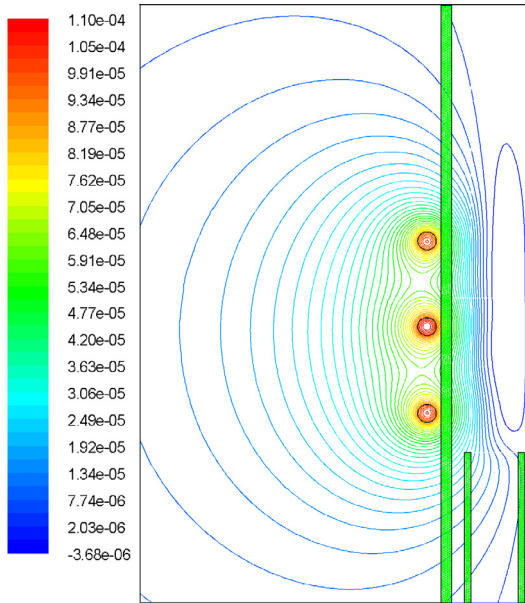


**Figure 15: DPBC Model** $A_{R\theta}$
**(T m)**
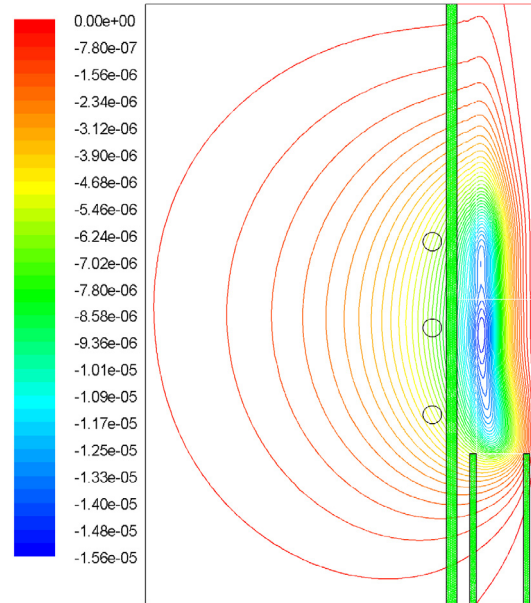
**Figure 16: DPBC Model** $A_{I\theta}$
**(T m)**

*1. Effects from Modeling the Q1 Region*

Large effects are seen in the temperature distribution and the stream function with the DPBC model. Figure 17, Figure 18, and Figure 19 give plasma results for including the Q1 region. The boundary condition for fluid flow along a wall is that the velocity be zero. Solving Navier-Stokes equations gives parabolic flow velocity through a pipe with a maximum at the center [31]. Modeling the flow through a pipe creates a type of jet in comparison to modeling a uniform velocity distribution through the cross section. An additional cause of this jet effect is the increase in temperature in the pipe.

In Figure 17, the temperature of argon from Q1 reaches roughly 4000K and over 30m/s in the center of the Q1 pipe by the time it reaches the plasma region (in the test model and the Sherbrooke model this is 300K and a little over 1.8m/s for comparison).

The increase in axial momentum at the inlet equates to modeling a higher axial velocity on-axis at the outlet. The effects of this can be seen in the highest temperature contours terminating on axis for the test model (Figure 8) and on the outlet for the DPBC model (Figure 17). Additionally, this implies that the bulk of the heat is lost through the outlet for the DPBC model and by radiative cooling for the test model. This can be seen in the integrated radiative heat loss values for the Sherbrooke, Test, and DPBC models in Table VI. The slower velocity in the test model allows the high temperature gas to cool substantially before exiting through the outlet boundary. In the DPBC model the gas doesn't have this much time. Therefore we see over 23 times more radiative heat loss modeled with the test model in comparison to the DPBC model.

**Table VI: Total Power Values**

|  | Total Integrated Power | Radiative Heat Loss |
|---|---|---|
| Sherbrooke Model | 5 kW | N/A |
| Test Model | 4.996284 kW | 1240.05 W |
| DPBC Model | 5.150548 kW | 52.7729 W |
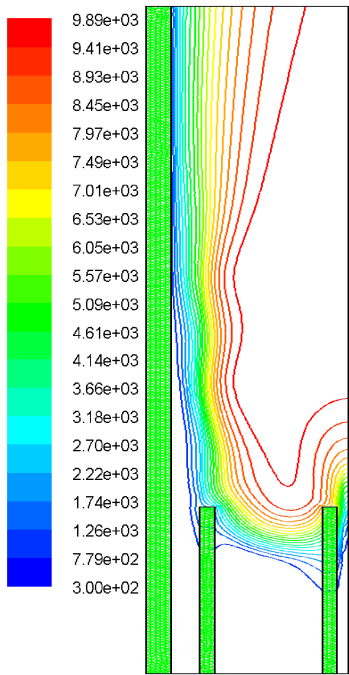
**Figure 17: DPBC Temperature (K)**
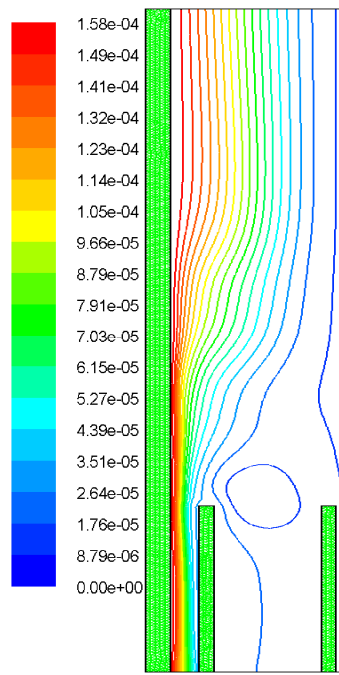
**Figure 18: DPBC Stream Function (kg/s)**
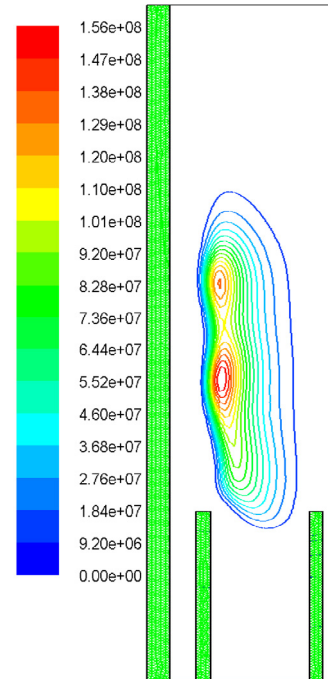
**Figure 19: DPBC Joule Heating** $W / m^3$

The higher velocity also explains the difference in peak temperature for the Sherbrooke, Test, and DPBC models (9920, 10002, and 9889 K respectively). Despite having more modeled integrated power, the DPBC model has a lower peak temperature because of higher velocity on axis. The maximum value for joule heating was increased slightly to $1.565 \times 10^8$ W/m$^3$ in Figure 19.

The DPBC effects are also seen in the stream function. For the test model, the streamline coming from Q1 goes up and over the turbulent region. This is from the argon momentum at Q1 being small and being absorbed into the turbulent clockwise flow surrounding the pipe. In Figure 18 for the DPBC model, the streamline coming from Q1 goes straight through the plasma region on the axis. This type of flow is modeled by a few independent groups [23, 40].

*2. Effects from Modeling with Dipole Boundary Conditions*

The effects from adding dipole boundary conditions are not as significant as modeling the Q1 region. The extrema from the DPBC model are slightly of higher magnitude in comparison to the values from a vanishing boundary condition at the walls. This is expected because the vector potential no longer must conform to unnaturally vanishing boundary conditions for field. The higher field effects can be seen in the total integrated power values for the Sherbrooke, Test, and DPBC models. The dipole boundary condition produced 3% more modeled integrated power and 1% higher peak power.

## D. Concluding Remarks

The results from the test model are in close agreeance with the 2-D Sherbrooke model. The bulk of the differences arose from the test model having a slightly smaller mesh size and therefore more precise results. The largest difference was in the maximum values of joule heating. However, the total integrated power had less than a tenth of a percent difference. Under the given assumptions, the 2-D simulation code performed as expected in comparison to the Sherbrooke model. By adding dipole boundary conditions and modeling the flow and heat transfer near the Q1 inlet, we improved the realistic nature of the model simulation. Several of the properties changed but not drastically. The effects are most easily explained by higher flow momentum at the Q1 inlet.

The goal of modeling an inductively-coupled RF plasma was to see if non-turbulent, laminar flow would occur in the entire plasma region. With the 2-D results, we may claim that the answer is yes. However, to simplify the model, we modeled an axis-symmetric geometry and completely azimuthal driving current loops. The asymmetries associated with the actual copper driving coils have the largest effect on the flow characteristics in the plasma [17, 24, 41]. Therefore, a fully 3-D theory and model must be developed to attempt to design a laminar RF plasma torch.

## IV. 3-D CODE VERIFICATION MODEL

In modeling an axis-symmetric geometry we have neglected the largest effects that would destroy the symmetry of laminar flow in the plasma exhaust plume. The asymmetries associated with the copper coil have the largest effect on the flow temperature, streamlines, and velocity. With three dimensional capability, we may potentially be able to design a torch to have completely laminar flow with little or no mixing.
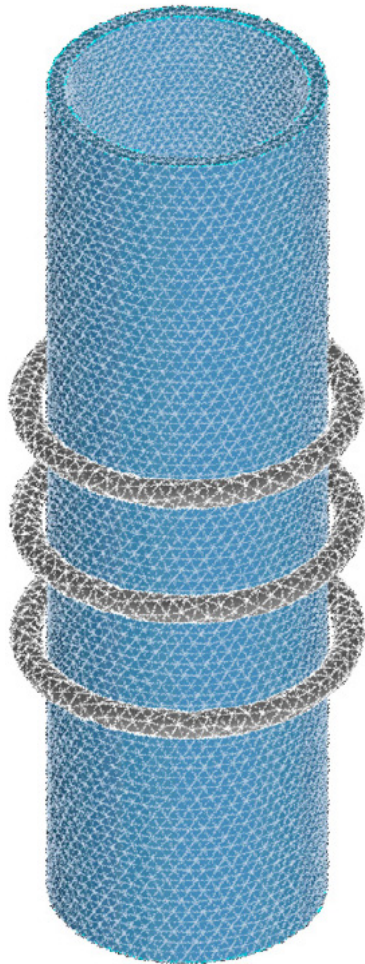


**Figure 20: Bologna Grid**                    **Figure 21: 3-D Test Model Grid**
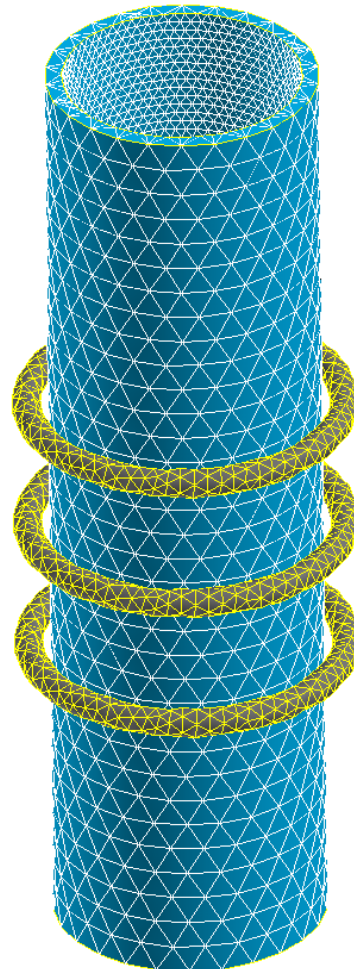
We must first verify that the three dimensional code will give comparable results to the two dimensional code. Therefore, our code verification model will be a 3-D representation of our 2-D test model. At the University of Bologna in Italy, they have published a comparable model to our 3-D test model [17].

In Figure 20 and Figure 21 we have a mesh from the Bologna group and our test model grid. The meshes were produced in GAMBIT$^©$ which is a preprocessor program for FLUENT$^©$. The Bologna Grid has $8.5 \times 10^3$ cells in the coil region, $10^5$ cells in the extended electromagnetic field region, and $3.5 \times 10^5$ cells in the plasma region. The 3-D Test Grid has $4.0 \times 10^3$ cells in the coil region, $2.8 \times 10^4$ cells in the extended electromagnetic field region and $2.5 \times 10^5$ cells in the plasma region. As the two figures reveal, the test model as fewer cells in the walls. However, in the important plasma region, the cell size is quite comparable.

The frequency of oscillation for the torch model is 3MHz. The input parameterization is the same as in the 2-D case as listed in the table on page 29. However, rather than setting the coil current, we will be setting the total integrated power dissipated to 5.00kW.

A. Setting Power Dissipated Versus Current

There are two reasons to converge the model to a set power rather than a set current. First of all, the power supply applies a set voltage across the coils and not a set peak current. Second, the plasma parameters are directly dependent upon the power dissipated rather than the current.

As discussed in Appendix A the plasma, the copper coils, and the power supply are all highly coupled together in terms of inductance or impedance. The total coil current is highly dependant upon this impedance. However, the power supply applies a set voltage to the coil. This is similar to setting the power applied to the coil plasma system. For a set resistance, power is proportional to voltage squared.

**Table VII: Converged Results for Comparison**

| Case | $I_0$ (A) | Power (kW) | T (K) | Max $A_{R\theta}$ (T m) | Min $A_{I\theta}$ (-T m) | MaxJoule (W/m$^3$) | $\vec{v}$ (m/s) |
|---|---|---|---|---|---|---|---|
| 2-D Test Case | 161 | 4.996 | 10002 | $1.101\times10^{-4}$ | $1.477\times10^{-5}$ | $1.55\times10^{8}$ | 17.21 |
| Coarse Set $I_0$ | 161 | 1.969 | 9672 | $9.33\times10^{-5}$ | $9.29\times10^{-6}$ | $5.97\times10^{7}$ | 9.24 |
| %Error | 0% | 60% | 3% | 15% | 37% | 61% | 46% |
| Coarse Set Power | 196.6 | 5.000 | 9836 | $1.06\times10^{-5}$ | $1.44\times10^{-5}$ | $1.24\times10^{8}$ | 16.77 |
| % Error | 22% | 0% | 1.7% | 4% | 3% | 20% | 3% |
| Fine Set $I_0$ | 161 | 3.284 | 9807 | $9.79\times10^{-5}$ | $1.26\times10^{-5}$ | $1.02\times10^{8}$ | 13.94 |
| % Error | 0% | 34% | 2% | 11% | 15% | 34% | 19% |
| Fine Set Power | 184.6 | 5.000 | 9998 | $1.104\times10^{-5}$ | $1.46\times10^{-5}$ | $1.44\times10^{8}$ | 17.42 |
| % Error | 15% | 0% | 0.04% | 0.3% | 1.2% | 7% | 1.2% |

As a rough preliminary test, a coarse 3-D grid with $2.1\times10^{4}$ total cells was constructed with the same geometry as the figure on page 28 and same parameters as the table on page 29. The fine case is the results from the 3-D test mesh from Figure 21. Table VII gives converged values for various flow variables for a set-current case and the set-power case. The percent error is with respect to the 2-D Test Model.

The percent errors are smaller across the board when the power is set as opposed to the current. These results imply that some of the grid dependences on results are removed by simply setting the power rather than the current.

### 1. Mesh Dependence

In this chart we also see a strong dependence on the mesh size. A good parameter to compare meshes is a characteristic length ($l$) given by:

$$l = \sqrt{\overline{cell\ Area}} = \sqrt{\frac{total\ Area}{\#cells}} \tag{80}$$

in the 2-D case and for the 3-D case we have the following:

$$l = \left(\overline{cell\ Volume}\right)^{\frac{1}{3}} = \left(\frac{total\ Volume}{\#cells}\right)^{\frac{1}{3}}. \tag{81}$$

Table VIII gives a summary of the characteristic mesh lengths for the 2-D Test model, the coarse 3-D mesh, and the 3-D Test Model. The data points only incorporate the plasma region.

**Table VIII: Characteristic Mesh Lengths**

| Case | Characteristic Length (m) |
|------|---------------------------|
| 2-D Test-Model Case | $3.4 \times 10^{-4}$ |
| 3-D Test-Model Case | $1.24 \times 10^{-3}$ |
| 3-D Coarse-Mesh Case | $3.80 \times 10^{-3}$ |

There is a definite correlation between the characteristic length and most of the fluid variables listed in Table VII. See Appendix D for a graphical representation of Table VII and Table VIII.

For the set-current cases, as the characteristic length decreases, the maximum values for flow and field increase strongly. However, for the set-power cases the correlation is much weaker. Therefore, by setting the power dissipated in the plasma

region we are more able to standardize and compare results between models and decrease the dependence on mesh size.

There are some converging issues that are special to setting the power dissipation rather than the current. In the governing electromagnetic equations, the current is treated as a constant. Therefore, if we change the current, then the energy equation and the vector potential equation must be close to converged before the current may be accurately changed again. In practice, this extra procedure doubles the number of iterations required before convergence. For equation (79), a converged value residue is considered to be $10^{-6}$ or less. Therefore, a converged total power value would be 0.005 Watts/ $m^3$ deviated from 5000 Watts/$m^3$.

The flow chart changes slightly for the 3-D solver. For setting the dissipated power, a User Defined Function was written. The UDF is run at the beginning of each iteration and decides if the energy and vector potential equations have converged enough to calculate the integrated power. After the total power is calculated, the result is used to adjust the amount that the current changes. The change is proportional to the difference between the target power and the calculated power as the following equation:

$$I_{new} = I_{old} + \beta \left( P_{target} - P_{calculated} \right) \tag{82}$$

where $\beta$ is the dissipation parameter. The dissipation parameter will adjust if the subsequent change in total power is too large or too small. A new flow chart of how the 3-D UDF code works is given in Figure 22.

## B. Under-Relaxation Factors

The under-relaxation factors defined in equation (74) are largely the same for the 3-D test model. However, the under-relaxation factor for the 6 vector potential equations may be greatly increased. With no singularity involved, the values may be safely set to 0.96 at initialization and increased to 0.99 after 1000 iterations. This drastically decreased the required number of iterations before the vector potential would converge as discussed with equation (77). Conversely, the scalar potential has a very complicated

source term in the plasma region. The gradient of the conductivity multiplied by the gradient of the scalar potential is very unstable.

The under-relaxation parameter for the scalar potential must be smaller than $2 \times 10^{-8}$ so that the iterations don't diverge. However, in the 3-D test case, the *z*-component of vector potential and the scalar potential equations were neglected to only include what was modeled in the 2-D test case. However, since the current is still azimuthal and thus not axial electric field for current to collect. The inclusion of these equations would have no effect on the results. This was verified after the 3-D test case was converged.

## C. Judging Convergence

The residual values are comparable to the 2-D values listed in the table on page 35. The one notable difference arises with the mass continuity residue. The value converged much more in the 3-D test case. The residues are summarized in Table IX.

**Table IX: 3-D Test Model Residues**

| Mass Continuity | Axial Momentum | Radial Momentum | Energy | $\phi$ | $\vec{\mathbf{A}}_R$ | $\vec{\mathbf{A}}_I$ |
|---|---|---|---|---|---|---|
| $2.0 \times 10^{-11}$ | $2.5 \times 10^{-8}$ | $1.0 \times 10^{-8}$ | $2.5 \times 10^{-8}$ | $1.2 \times 10^{-4}$ | $2.5 \times 10^{-10}$ | $1.0 \times 10^{-9}$ |

The residues for the real *x* and *y* components of vector potential had the same value and are listed collectively as $\vec{\mathbf{A}}_R$. The same is true for radial momentum and the imaginary *x* and *y* components of vector potential. The residue for scalar potential was converged to $1.2 \times 10^{-4}$. The scalar potential residue is larger because of the non-linearity of the source terms in equation (63) and the extremely small under-relaxation factor ($2 \times 10^{-8}$).
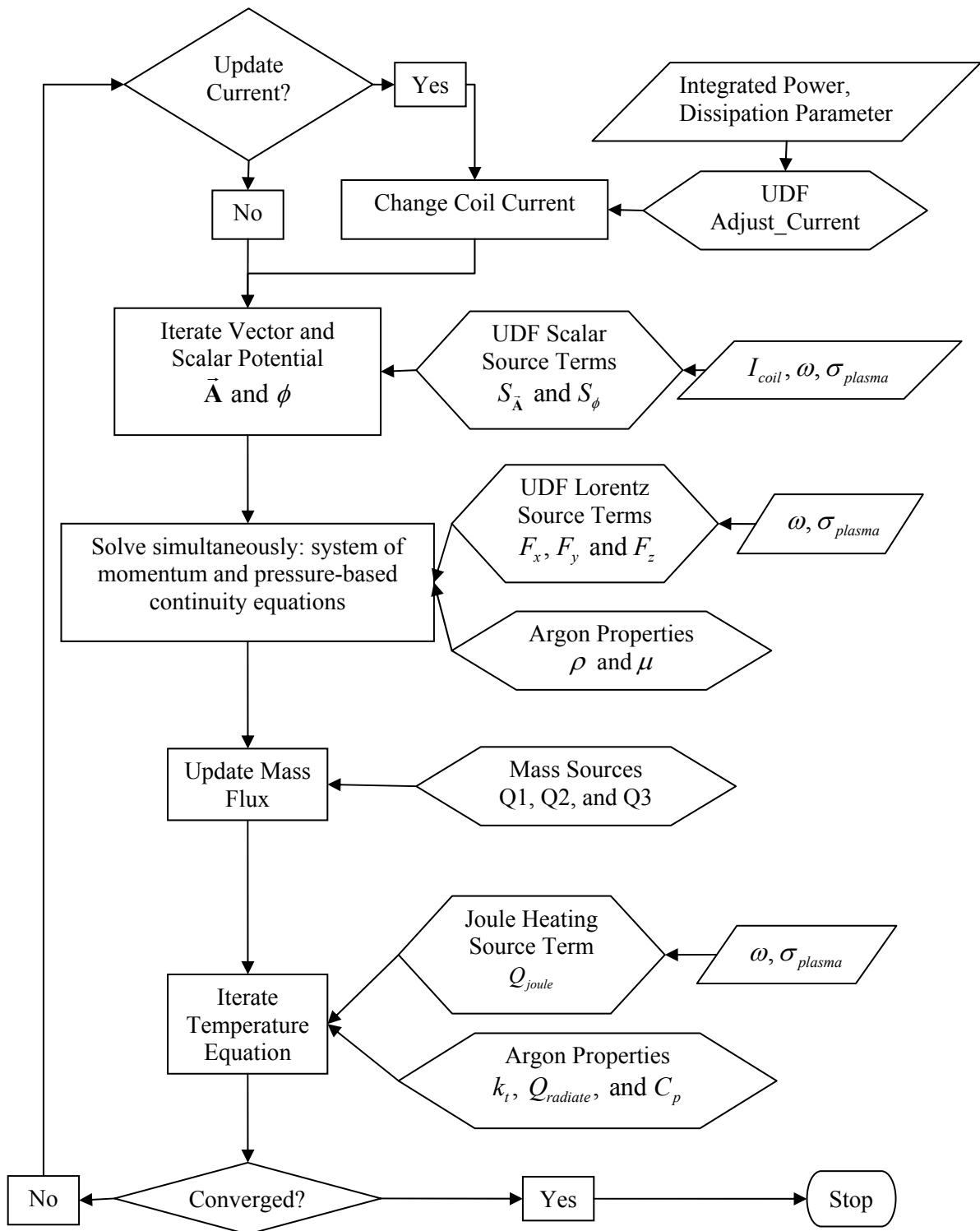
**Figure 22: Flow Chart for the 3-D Coupled Pressure-Based Solver**

The flow and vector potential variables were converged after roughly 20,000 iterations. This is roughly half of the required number for the 2-D test model. The vector potential equations having more stability in Cartesian coordinates enabled this number to decrease. However, because the total number of cells was nearly tripled, the total CPU hours increased proportionately.

## D. Results

### *1. Temperature Profiles*

The temperature profiles of the two comparable models are very similar. The only differences occur in the maximum value and the inverted areas at the Q1 region and the exit plume region. The two temperature color profiles in Figure 23 and Figure 24 are slightly different. The red, green and blue contour lines of the Bologna distribution are more contrasted than the 3-D test model.

The maximum temperature of the Bologna model is 9922K and the maximum temperature of the 3-D test model is 9998K. The difference between the 2-D case and the Sherbrooke model has almost the same characteristic difference despite having almost identical temperature contour shape. The difference is small at less than a percent, but there most likely is some differing parameter that the author isn't aware about that might be causing this systematic error. At this time the cause is unknown. The origin of this discrepancy (along with joule heating) should be found before any design or construction of a torch.

Another difference between the two temperature profiles is the region of concavity of the highest contour line in the 3-D test model. The Bologna distribution doesn't contain this feature both in the exit plume and at the Q1 region. The 3-D test model does contain the feature. In both 2-D cases the concave contour is included. Therefore, I am fairly confident that the 3-D model is correct in simulating a concave region of slightly lower temperature both in the exit plume and at the Q1 inlet.
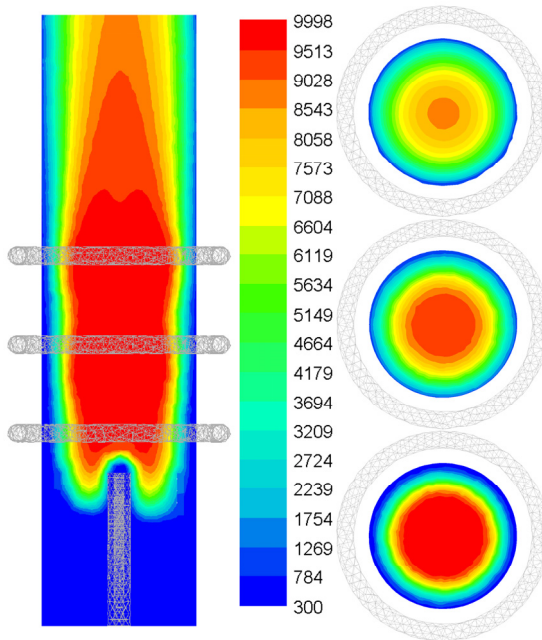
**Figure 23: 3-D Test Model Temperature Profiles (K)**
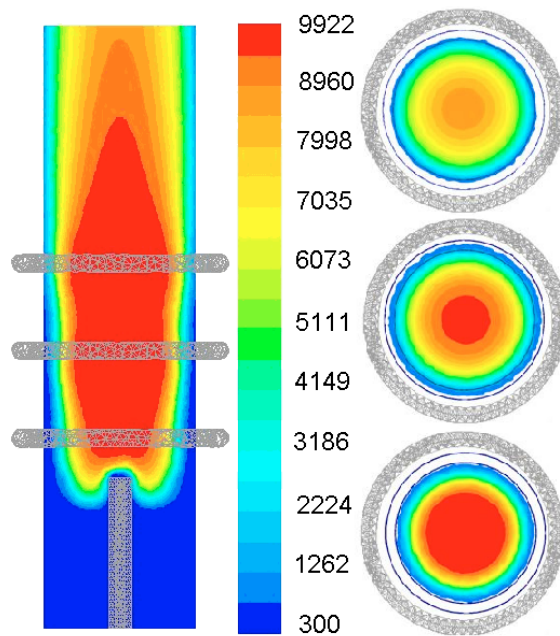
**Figure 24: Bologna Temperature Profiles (K)**

## 2. Velocity Profiles

The velocity profiles have very similar shape. Just like in the temperature profiles, the Bologna model has a well defined red, green and blue contour line in comparison to the 3-D test model. This difference causes there to appear a drastic difference in the velocity contours. However, the shape of the contour lines are quite similar.

There is a slight difference in the maximum velocity with 17.42 m/s in the 3-D test model in Figure 25 and 16.64 m/s in the Bologna model in     Figure 26. The potential causes of this slight discrepancy are discussed with the swirl velocity and gravity subsections. However, the 2-D model at 17.21 m/s, has a maximum velocity that is very close to our 3-D model.
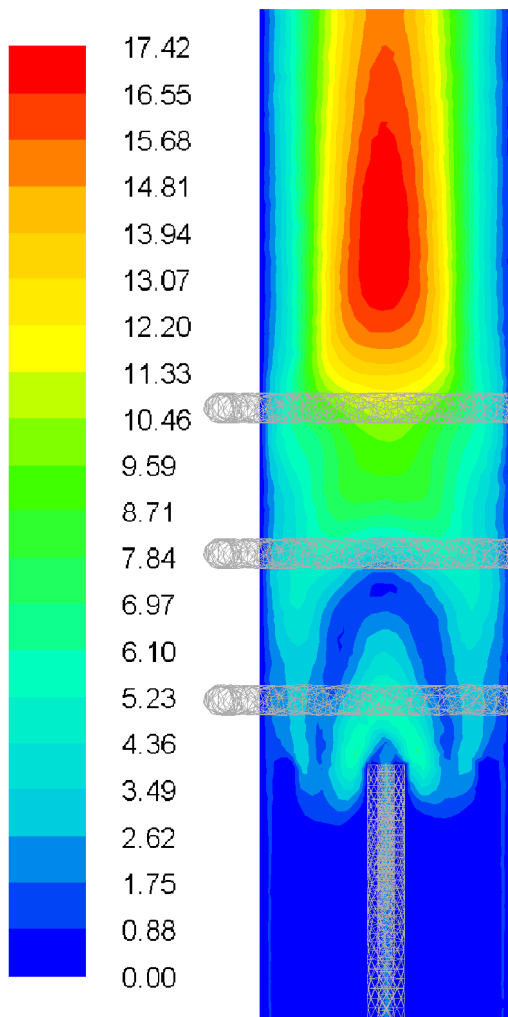
**Figure 25: 3-D Test Model Velocity Profile (m/s)**
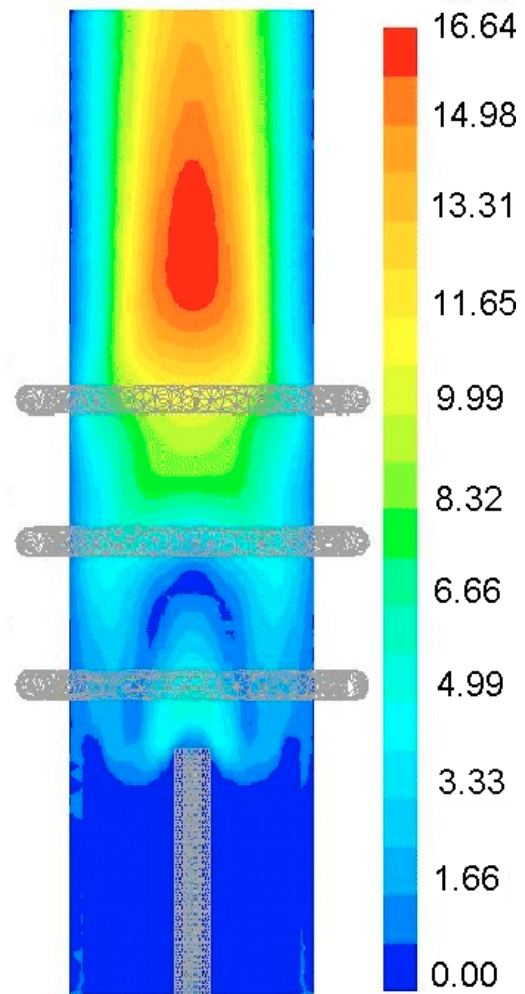
**Figure 26: Bologna Velocity Profile (m/s)**

## 3. Joule Heating Profiles

The joule heating profiles are quite comparable as in the temperature and velocity distributions. However, maximum values are once again different at $1.58 \times 10^8$ W/m$^3$ in Figure 27 and $1.44 \times 10^8$ W/m$^3$ in Figure 28. The maximum joule heating in the Sherbrooke 2-D model and the 2-D test model was $1.41 \times 10^8$ W/m$^3$ and $1.55 \times 10^8$ W/m$^3$ respectively. The differences are somewhat acceptable given that the total integrated joule heating or total power dissipated for each model is the same value at 5.00 kW.

Despite having correct shape, the top 4 contour levels aren't visible in the Bologna model. The highest values of joule heating are found at locations not on the cross sectional slice chosen by the Bologna group. This implies that the output for joule heating of their model is asymmetric to a small degree. The maximum contour shown by the Bologna cross section appears to be $1.11 \times 10^8$ W/m$^3$. This is quite a large difference in comparison to the actual maximum joule heating value.
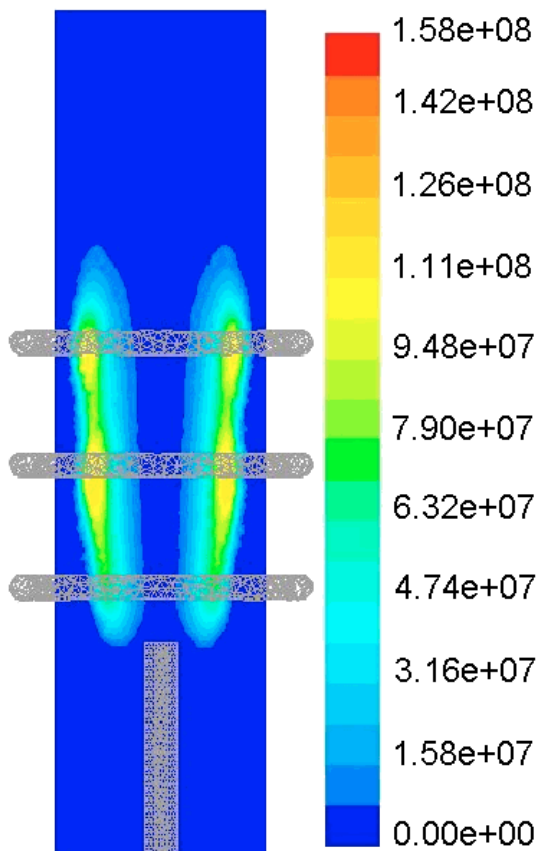


**Figure 27: Bologna Joule Heating Profile** $W / m^3$
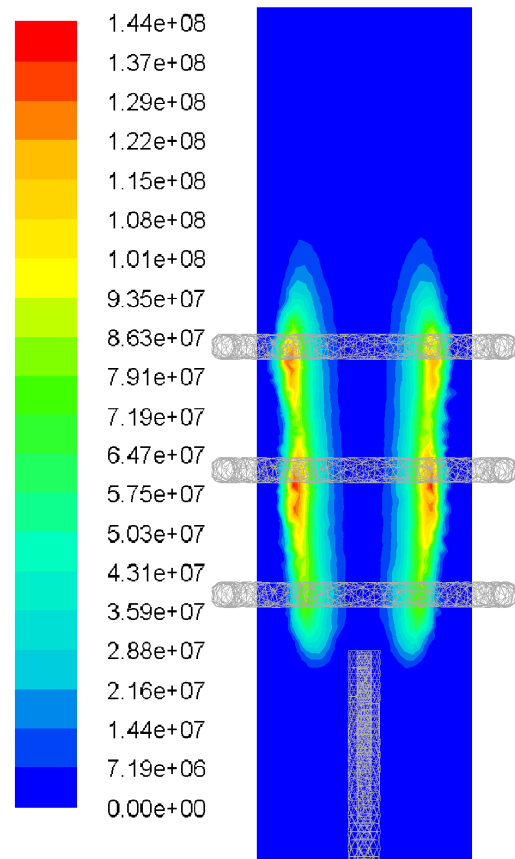
**Figure 28: 3-D Test Model Joule Heating Profile** $W / m^3$

*4. Swirl Velocity*

The 3-D test model had the same dimensions and symmetries as the 2-D model. Therefore, from it we can't glean any new information about the amount of mixing in the plasma region as caused directly by asymmetries in the coil currents. In the 2-D axis symmetric model all tangential or swirling velocities were assumed null because there were no tangential forces. (Axial current, in addition to azimuthal current, is required for theoretical tangential Lorentz forces.) Therefore, in the 3-D analog of the 2-D test model, there should not have been any theoretical tangential forces to cause swirling. However, we were able to see some effects from removing the azimuthal restraint in the 3-D test model. The 3-D model gave a maximum swirling velocity of 0.47 m/s near the Q1 outlet where the velocity magnitude is roughly quadruple that amount. In the outer sheath region the maximum swirl velocity is about 0.08 m/s and the velocity magnitude is 4 m/s. This area of the torch is of importance in designing the torch for laminar, non-mixing flows. Theses numbers are quite small and shouldn't directly destroy laminar flow.

Now we must ask ourselves of the source of these swirling velocities that might destroy laminar flow. Without axial current the theoretical tangential swirl velocity should be zero. However, there is a negligible but non-zero amount of tangential force that is about $1/25^{th}$ of the total force. These forces might arise from mesh effects. When modeling in 3-D the mesh isn't quite perfectly cylindrical. Each cell face is planar and thus it's impossible to make a perfect 3-D mesh with cylindrical symmetry. As the cells get smaller these aberrational effects should diminish. However, with a coarser mesh the swirl velocity is still around 0.5 m/s. Therefore, it appears that the origin of the swirl velocity isn't directly from the mesh.

These small swirl velocity artifacts may be arising from the cell order in the iterative process. FLUENT© doesn't specify the cell order by which each iteration takes place. If the ordering is circular then we might have a remnant circling velocity. If the ordering is linear we might see a remnant linear velocity in the direction of the ordering. FLUENT© does allow the cell ordering to be altered to optimize memory usage.

However, we can't specify how the reordering takes place so that artificial velocities are minimized. A completely converged result shouldn't include any effects from the cell iteration ordering unless swirling velocities solve the fluid dynamical equations best.

Large swirling velocities may potentially result in mixing or turbulence in the plasma region. In future models we must be extremely careful to design the coils to minimize this component of flow. It's difficult to give a graphical representation of the swirl velocity because the software doesn't offer a streamline mass function in three dimensions.

## 5. Gravity Inclusion

The inclusion of the force of gravity may affect our results. Both the Sherbrooke and the Bologna groups did not mention that gravity was included in their simulation. For the 2-D and 3-D test models, gravity was not accounted for. The effects of its inclusion potentially could be seen in the velocity distribution. Any small change in the flow could certainly result with different maximum values in temperature and joule heating. Before future models are simulated, we must add gravity as a source term in the force equation to these models to verify its effects and once again compare results.

Converged results of the 2-D test model with the inclusion of gravity show rather large effects. The maximum velocity changed from 17.21 m/s to 17.29 m/s in the plasma region. This may be explained by the cooler, denser gas near the walls squeezing the central core plasma. This squeezing has resulted in slightly larger velocities. The higher velocities decrease the time spent by the gas in the joule heating region and thus the temperature reduces from 10,002K to 9,979K. Additionally, the maximum joule heating amount decreased to $1.49 \times 10^8$ W/m$^3$ from $1.55 \times 10^8$ W/m$^3$. The maximum temperature and joule heating shifted closer to the Sherbrooke and Bologna model values while the velocity moved further away. Therefore, the results are inconclusive whether the neglect of gravity is the main culprit for differences between the 3-D test model and the Bologna model.

E. Concluding Remarks

The results of our 3-D test model have very close results in comparison to other comparable 3-D models. Additionally, the results are in excellent agreement with our 2-D counterpart. The results of this 3-D test model have verified the validity of the written user defined function source terms as well as the initialization conditions set up in FLUENT$^©$ for 3 dimensions. The results of the 3-D test model should give confidence as to any subsequent results for different coil geometries.

A few small discrepancies still remain between our models and the simulation results from the Sherbrooke group in Canada and the Bologna group in Italy. Our models have a maximum temperature that is roughly 80K larger. Our simulation has maximum velocities that are roughly 0.8 m/s faster vertically. One possible explanation is that they included gravity in their model. Another explanation for different results is the differing grids. As can be seen in the discussion of characteristic length in equation (80), the mesh has a significant effect on the flow and field variables. However, this effect should be minimized by setting the power rather than the current as discussed on page 49. Therefore, the mesh shouldn't be a significant cause of flow and field differentials.

# V. SUMMARY

## A. Modeling Conclusion

The flow in the 3-D case remained laminar as was seen in the 2-D case. This gives promise that as we wisely add components to the simulation, we may be able to keep the same characteristic non-mixing flow. Therefore, as a next step, we need to create a mesh with helixical coils. In this model we will need to optimize the coil angle to prevent plasma mixing and keep the coils separated enough to prevent arcing.

The next step would be to create a mesh with coil leads. The coil leads are the primary source of asymmetry for the plasma flow. Therefore, the most significant cause of mixing will be the addition of coil leads. The coil angle mostly causes tangential velocity in the plasma region but no mixing to a first approximation. The radial currents associated with the coil leads will cause direct turbulence and mixing in the plasma sheath.

The design of the torch in this step may be the most important to constructing laminar flow. The final component to modeling the plasma will be to add particles. We will need to model the inertial forces associated with aerosols as well as the viscous forces. This step will be crucial in predicting exactly how much mixing will occur between aerosols. Even if the argon flow as designed and modeled is completely laminar and non-mixing, the aerosol particles may still mix due to the individual particle momentum through curves. A full analysis of Stokes number associated with the aerosols will need to be conducted.

## B. Further Research

After modeling and designing the inductively-coupled plasma torch it will need to be constructed and characterized. The temperature profile may be analyzed by Atomic Emission Spectroscopy (AES) and the flow may be monitored by pulsed laser photography of aerosol flow. With this data we may adjust flow rates and power supply parameters to specifications that minimize turbulence and mixing. We must also design

and construct a roller system for coating the silicon carbide strands for use in a metal matrix composite fuel cladding.

## REFERENCES

[1]     NRC, *Expected New Power Plant Applications*, edited by DOE (Nuclear Regulatory Commission, 2008), www.nrc.gov/reactors/new-licensing/new-licensing-files/expected-new-rx-applications.pdf.

[2]     C. Savage, and J. Kelly, *Advanced Fuel Cycle Initiative Program Plan*, edited by DOE (AFCI, 2007),

http://afci.sandia.gov/downloads/2005_AFCI_Program_Plan.pdf.

[3]     K. Devan, G. Pandikumar, M. A. V. Gopalakrishnan, and P. Mohanakrishnan, Annals of Nuclear Energy **30**, 17 (2003).

[4]     R. G. Pahl, C. E. Lahm, and S. L. Hayes, Journal of Nuclear Materials **204**, 7 (1993).

[5]     D. Smith, P. McIntyre, B. Basaran, and M. Yavuz, *SiC Composite: A New Fuel Cladding for High-Temperature Cores* (Texas A&M University, College Station, TX, 2003), p. 3 (unpublished).

[6]     T. Elliott, P. McIntyre, and A. Sattarov, in Proceedings of the Applied Superconductivity Conference, Seattle, WA, 2006, p. 4, edited by H. Kumakura, and A. Matsumoto.

[7]     D. Smith, and P. McIntyre, *Steel-SiC Metal Matrix Composite Development* (Texas A&M University, College Station, TX, 2004), p. 16 (unpublished).

[8]     P. McIntyre, *Virtual-Impact Particle Sizing for Precursor Powders* (Texas A&M University, College Station, TX, 2006), p. 47 (unpublished).

[9]     A. McFarland, P. McIntyre, and S. Seshadri, in Proceedings of the Applied Superconductivity Conference, Jacksonville, FL, 2006, edited by D. Dietderich.

[10]    M. I. Boulos, Pure Applied Chemistry **68**, 4 (1996).

[11]    F. Gitzhofer, Pure Applied Chemistry **68**, 8 (1996).

[12]    E. Rajamaki, T. Varis, A. Vaidya, A. Kulkarni, M. Karadge, J. Gutleber, S. Sampath, and H. Herman, in Proceedings of the International Thermal Spray Conference, Essen, Germany, 2002, edited by E. Lugscheider.

[13]    J. P. Mellado-Gonzalez, *Development of a Chemical Kinetics Model for Inductive Plasma Simulations* (von Karman Institute for Fluid Dynamics Report, St.Genése-Rode, Belgium, 1998) (unpublished).

[14]    A. E. Mensing, and L. R. Boedeker, *Theoretical Investigations of RF Induction Heated Plasmas* (NASA Report, East Hartford, CT, 1969) (unpublished).

[15]    R. C. Miller, and R. J. Ayen, Journal of Applied Physics **40**, 1 (1969).

[16]    D. V. Abeele, S. A. Vasilevskii, A. F. Kolesnikov, G. Degrez, and B. Bottin, *Code-To-Code Validation of Inductive Plasma Computations* (von Karmon Institute for Fluid Dynamics Report, St.Genése-Rode, Belgium, 1999), p. 27 (unpublished).

[17]    D. Bernardi, V. Colombo, E. Ghedini, and A. Mentrelli, The European Physical Journal D **22**, 7 (2003).

[18]    D. Bernardi, V. Colombo, E. Ghedini, and A. Mentrelli, The European Physical Journal D **27**, 18 (2003).

[19]    V. Colombo, C. Panciatichi, A. Zazo, G. Cocito, and L. Cognolato, IEEE Transactions on Plasma Science **25**, 8 (1997).

[20]    W. L. T. Chen, J. Heberlein, and E. Pfender, Plasma Chemistry and Plasma Processing **16**, 16 (1996).

[21]    X. Chen, and E. Pfender, Plasma Chemistry and Plasma Processing **11**, 26 (1991).

[22]    J. McKelliget, and N. El-Kaddah, Journal of Applied Physics **64**, 7 (1988).

[23]    J. McKelliget, J. Szekely, M. Vardelle, and P. Fauchais, Plasma Chemistry and Plasma Processing **2**, 16 (1982).

[24]    D. Bernardi, V. Colombo, E. Ghedini, and A. Mentrelli, Pure Applied Chemistry **77**, 14 (2005).

[25]    S. Xue, P. Proulx, and M. I. Boulos, J. Phys. D: Appl. Phys. **34**, 10 (2001).

[26]    S. Xue, P. Proulx, and M. I. Boulos, Plasma Chemistry and Plasma Processing **23**, 19 (2003).

[27]    Fluent, *FLUENT 6.3 Documentation* (ANSYS, Inc., Lebanon, NH, 2006).

[28]   D. V. Gravelle, M. Beaulieu, M. I. Boulos, and A. Gleizes, Journal of Physics D: Applied Physics **22**, 7 (1989).

[29]   J. J. Bloomer, *Practical Fluid Mechanics for Engineering Applications* (Marcel Dekker, Inc., New York, 2000), p. 408.

[30]   F. M. White, *Fluid Mechanics* (McGraw-Hill, Boston, 1998), p. 1023.

[31]   L. D. Landau, and E. M. Lifshitz, *Fluid Mechanics* (Pergamon Press, New York, 1987), p. 551.

[32]   P. M. Bellan, *Fundamentals of Plasma Physics* (Cambridge University Press, New York, 2006), p. 547.

[33]   S. Ichimaru, *Basic Principles of Plasma Physics: A Statistical Approach* (The Benjamin/Cummings Publishing Company, Inc., Reading, MA, 1980), p. 324.

[34]   J. D. Jackson, *Classical Electrodynamics* (Academic Press, New York, 1999), p. 808.

[35]   R. Fitzpatrick, *Introduction to Plasma Physics: A Graduate Course* (University of Texas, Austin, 2006), p. 242 (unpublished).

[36]   Fluent, *GAMBIT 2.3.16* (ANSYS, Inc., Lebanon, NH, 2006), CFD Meshing Software.

[37]   Fluent, *FLUENT 6.3.26* (ANSYS, Inc., Lebanon, NH, 2006), CFD Software.

[38]   S. Xue, Graduate Student (private communication, University of Sherbrooke, Quebec, 2008).

[39]   D. Bernardi, V. Colombo, G. G. M. Coppa, and A. D'Angola, The European Physical Journal D **14**, 12 (2001).

[40]   D. V. Abeele, and G. Degrez, American Institute of Aeronautics and Astronautics **38**, 9 (2000).

[41]   S. Sampath, CTSR Director (private communication, University of Stony Brook, NY, 2008).

## APPENDIX A: INDUCED COIL CURRENT DISCUSSION

The current density for three 6mm wires at 250Amps (750 Amps total) is $2.2 \times 10^6$ Amps/meter$^2$. The maximum induced current density in the plasma is roughly (from converged data from 250 Amps) from (18) is:

$$\left| \vec{\mathbf{J}}_{ind} \right|_{max} = \omega \sigma \sqrt{\vec{\mathbf{A}}_{max} \bullet \vec{\mathbf{A}}_{max}} \approx 1.3 \times 10^6 \text{ Amps/meter}^2 \qquad (83)$$

where the ½ factor is from time averaging (see explanation to (33)). However, if we integrate this value over the plasma region, then the total current would be:

$$I_{plasma} = \int \vec{\mathbf{J}}_{ind} \bullet d\vec{\mathbf{A}} = 945.4 \text{ Amps.} \qquad (84)$$

Therefore the total current in the plasma region is roughly of the same order as the total current in the coils. Now in actuality, the induced currents themselves are going to induce currents in the conductive coils. However, because the direction of $I_{plasma}$ is azimuthal and smoothly distributed, the currents in the plasma region can be considered to a fair approximation as a solenoid where the field outside is zero. Therefore the induced current in the coils will be an order of magnitude smaller than the 250 Amp coil driving current.

We may to a first approximation, estimate the plasma as a single loop in the same plane as a coil loop. Proceeding we may theoretically calculate the contributions to the coil current. Writing the potential drops across the Kirchhoff coil loop we have the following:

$$I_{coil} R_{coil} + \frac{\partial}{\partial t}\left( M_{c,p} I_{plasma} \right) + \frac{\partial}{\partial t}\left( L_{coil} I_{self,coil} \right) = V(t) \qquad (85)$$

where the mutual inductance between the coil and the plasma loop is $M_{c,p}$, $L_{coil}$ is the self inductance of the coil, and $R_{coil}$ is the total resistance of one coil loop. The first term represents the voltage drop from the driving current through the coils. The second term is the voltage drop due to the mutual inductance between the plasma and the coils. The third term is the voltage drop from the coils self inductance. The self inductance of a thin wire loop at high frequency can be written as the following:

$$L_{coil} = \frac{\mu_0 a_{coil}}{4} \approx 1.04 \times 10^{-8} \, \text{H}$$ (86)

where $a_{coil}$ is the loop radius. If $\delta$ is the skin depth for copper given by:

$$\delta = \sqrt{\frac{2}{\mu_0 \omega \sigma}} \approx .04 \, \text{mm (Jackson 1999)}$$ (87)

then the resistance may be written from the cross sectional conduction skin as the following:

$$R_{coil} = \frac{length}{\sigma \, Area} = \frac{2\pi a_{coil}}{\sigma 2\pi r_{coil} \delta} = \frac{a_{coil}}{\sigma r_{coil} \delta}$$ (88)

The mutual inductance between any 2 circuits may be written as the following:

$$M_{2,1} = M_{1,2} = \frac{1}{I_1} \oint \vec{A}_{1,2} \cdot d\vec{l} = \frac{1}{I_2} \oint \vec{A}_{2,1} \cdot d\vec{l} \text{ (Jackson 1999)}$$ (89)

where $\vec{A}_{1,2}$ is the vector potential of circuit 1 at circuit 2. Using the vector potential for a dipole in equation (28) we may solve the path integral to find that

$$M_{1,2} = \frac{\mu_0 \pi}{2} \left( \frac{r_1^2 r_2^2}{\left( r_1^2 + r_2^2 \right)^{3/2}} \right) \approx 1.02 \times 10^{-8} \, \text{H} \, .$$ (90)

Inductance in this case is largely geometrical and time independent (given the current distribution in the wire is frequency independent). Therefore the time derivatives in equation (85) may be replaced by $\omega$. Here we must be careful to differentiate between the self induced current ($I_{self,coil}$), the drive current ($I_{coil}$), the induced current in the coil from the plasma ($I_{COILind}$), and the induced current in the plasma ($I_{ind}$). Throughout this paper we assumed that $I_{coil}$ was 250 amperes. However, when we include the self inductance, the total current (in each coil) from the power supply and the self inductance is 250ampers or:

$$I_{coil} + I_{self,coil} = 250 \, \text{amperes.}$$ (91)

There is an inherent minus sign absorbed in $I_{self,coil}$ because it opposes the driving current according to Lenz's law. Assuming that $I_{plasma}$ is small so that if $I_{coil} \approx I_{self,coil}$, we may

estimate the contribution of the self inductance to the total current as the proportionality of the first over the last term in equation (85) as the following:

$$\frac{I_{coil}R_{coil}}{\frac{\partial}{\partial t}\left(L_{coil}I_{self,coil}\right)} = \frac{4}{\omega\sigma r_{coil}\delta\mu_0} \approx 0.025.$$ 

(92)

We may interpret this ratio as the fraction of $I_{coil}$ that contributes to the 250amps or:

$$.025I_{coil} \approx 250 \text{ amperes.}$$ 

(93)

This implies that for 250 amps to be flowing through the coil, then the generator must supply a voltage for $10^4$ coil amps if the self induced current is included. With this value for $I_{coil}$, the contribution to the total voltage by the plasma-coil coupling may be written as a ratio of the mutual inductance term over the other two terms as the following:

$$\frac{\frac{\partial}{\partial t}\left(M_{c,p}I_{plasma}\right)}{\frac{\partial}{\partial t}\left(L_{coil}I_{self,coil}\right)+I_{coil}R_{coil}} \approx \frac{\frac{\mu_0\pi}{2}\left(\frac{a_{coil}^2 a_{plasma}^2}{\left(a_{coil}^2+a_{plasma}^2\right)^{3/2}}\right)\omega I_{plasma}}{I_{coil}a_{coil}\left(\frac{\mu_0}{4}\omega-\frac{1}{\sigma r_{coil}\delta}\right)} = .095$$

(94)

where $r_{coil}=.003$ is the radius of the copper pipe, $a_{coil}=.015$, $a_{plasma}=.033$, and the conductivity of copper is $59.6\times10^6$ Siemens per meter. The minus sign in the denominator is because the self induced and driving currents oppose each other. This value implies that the induced current in the coil from the plasma ($I_{COILind}$) is roughly 10% of the total current (250 amps). From Lenz's law we know that the plasma will increase the current in the coils.

The above estimation doesn't take several influences into account. The inductance of an actual helixical copper coil is quite different than for a closed current loop. Also, when modeling 3 separate current loops, each loop might have severely different inductances which would alter the current coupling.

The difficulty in estimating the effects from mutual inductance from the plasma and the self inductance of the coil is obvious. With Vector Fields<sup>©</sup> (a powerful electromagnetic modeling software program) we modeled the plasma region as a slug of

metal with conductivity 2500 Siemens per meter. Using this conductivity as an estimate gives the closes fields and currents to that of modeling an argon plasma [26]. The results reveal that the actual effect for the induced coil current from the plasma is on the order of 16% and the self induced current in the coils is of the order of $2 \times 10^4$ amperes. The theoretical estimates above are roughly half these values. Vector Fields$^{©}$ also calculates a total coil inductance of $3.82 \times 10^{-7}$ H without a plasma. The same program models a total coil-plasma system mutual inductance of $3.3 \times 10^{-7}$ H with the plasma. These two numbers verify the theoretical trend of equations (86) and (90) with the self inductance larger than the mutual. However, these values are over 30 times larger than the theoretical values for single current loops. This arises because the numbers given from Vector Fields$^{©}$ incorporate the inductance of all three coils together (we would expect an $N^2 = 9$ factor). Regardless, if these two numbers replace the theoretical values of $L_{coil}$ and $M_{c,p}$ in equation (94), then we get the following result for the same equations:

$$\frac{\frac{\partial}{\partial t}\left(M_{c,p}I_{plasma}\right)}{\frac{\partial}{\partial t}\left(L_{coil}I_{self,coil}\right)+I_{coil}R_{coil}} \approx \frac{M_{c,p}\omega I_{plasma}}{I_{coil}\left(\omega L_{coil}-\dfrac{a_{coil}}{\sigma r_{coil}\delta}\right)} = .082 . \tag{95}$$

In actually modeling the plasma, we are most interested in the flow characteristics and temperature profile. These are definitely current and power supply dependent. However, with most RF power generators the frequency and current adjustments aren't well defined and have simple gross adjustment. Therefore the coil current we use in our model will simply be seen as a starting point for adjusting the power supply output.

## APPENDIX B: ARGON MATERIAL PROPERTIES

The following table is a continuous list of the material properties of Argon at atmospheric pressure from 300K to 13,200K. The data was acquired by a personal communication with an author of the Sherbrooke paper [38]. The temperature step is 100K and there are 130 data points for each property. The ordering and units are defined in Table X. The data was modeled as piecewise continuous. The data is graphically displayed in Figure 29.

**Table X: Data Ordering and Units**

| 1 | Viscosity $\mu$ | $\dfrac{kg}{m \cdot s}$ |
|---|---|---|
| 2 | Density $\rho$ | $\dfrac{kg}{m^3}$ |
| 3 | Thermal Conductivity $k_t$ | $\dfrac{W}{m \cdot K}$ |
| 4 | Specific Heat $C_p$ | $\dfrac{J}{kg \cdot K}$ |
| 5 | Electrical Conductivity $\sigma$ | $\dfrac{A}{V \cdot m}$ |
| 6 | Radiation energy loss rate $Q_{radiate}$ | $\dfrac{J}{s \cdot m^3}$ |

**Table XI: Temperature Dependant Data for Argon at 1atm**

| T(K) | $\mu$ | $\rho$ | $k_t$ | $C_p$ | $\sigma$ | $Q_{radiate}$ |
|---|---|---|---|---|---|---|
| 300 | 1.90190E-5 | 1.62260E+0 | 1.67310E-2 | 5.17570E+2 | 3.07840E-8 | 0.00000E+0 |
| 400 | 2.47400E-5 | 1.21690E+0 | 2.10020E-2 | 5.17350E+2 | 3.07840E-8 | 0.00000E+0 |
| 500 | 3.42240E-5 | 9.73530E-1 | 2.67120E-2 | 5.20330E+2 | 3.07840E-8 | 0.00000E+0 |
| 600 | 3.92450E-5 | 8.11210E-1 | 3.06310E-2 | 5.20630E+2 | 2.56100E-8 | 0.00000E+0 |
| 700 | 4.48580E-5 | 6.95300E-1 | 3.50110E-2 | 5.20530E+2 | 3.75550E-8 | 0.00000E+0 |
| 800 | 4.97420E-5 | 6.08390E-1 | 3.82230E-2 | 5.20480E+2 | 3.79030E-8 | 0.00000E+0 |
| 900 | 5.39210E-5 | 5.40790E-1 | 4.17850E-2 | 5.20440E+2 | 3.91360E-8 | 0.00000E+0 |

**Table XI: Continued**

| | | | | | | |
|---|---|---|---|---|---|---|
| 1000 | 5.76330E-5 | 4.86720E-1 | 4.49820E-2 | 5.20410E+2 | 3.92160E-8 | 0.00000E+0 |
| 1100 | 6.10760E-5 | 4.42480E-1 | 4.76690E-2 | 5.20390E+2 | 3.82000E-8 | 0.00000E+0 |
| 1200 | 6.43740E-5 | 4.05610E-1 | 5.02430E-2 | 5.20380E+2 | 3.66200E-8 | 0.00000E+0 |
| 1300 | 6.75980E-5 | 3.74410E-1 | 5.29600E-2 | 5.20370E+2 | 3.50180E-8 | 0.00000E+0 |
| 1400 | 7.07870E-5 | 3.47670E-1 | 5.52490E-2 | 5.20360E+2 | 3.38050E-8 | 0.00000E+0 |
| 1500 | 7.39600E-5 | 3.24500E-1 | 5.77250E-2 | 5.20360E+2 | 3.32720E-8 | 0.00000E+0 |
| 1600 | 7.71250E-5 | 3.04220E-1 | 6.01950E-2 | 5.20350E+2 | 3.36680E-8 | 0.00000E+0 |
| 1700 | 8.02840E-5 | 2.86330E-1 | 6.26610E-2 | 5.20350E+2 | 3.52690E-8 | 0.00000E+0 |
| 1800 | 8.34370E-5 | 2.70420E-1 | 6.51220E-2 | 5.20340E+2 | 3.84210E-8 | 0.00000E+0 |
| 1900 | 8.65820E-5 | 2.56190E-1 | 6.75760E-2 | 5.20340E+2 | 4.35190E-8 | 0.00000E+0 |
| 2000 | 8.97150E-5 | 2.43380E-1 | 7.00220E-2 | 5.20340E+2 | 5.07990E-8 | 0.00000E+0 |
| 2100 | 9.28340E-5 | 2.31790E-1 | 7.24560E-2 | 5.20340E+2 | 5.96870E-8 | 0.00000E+0 |
| 2200 | 9.59350E-5 | 2.21260E-1 | 7.48770E-2 | 5.20340E+2 | 6.77640E-8 | 0.00000E+0 |
| 2300 | 9.90170E-5 | 2.11640E-1 | 7.70820E-2 | 5.20330E+2 | 7.09740E-8 | 0.00000E+0 |
| 2400 | 1.02080E-4 | 2.02820E-1 | 7.91690E-2 | 5.20330E+2 | 6.70650E-8 | 0.00000E+0 |
| 2500 | 1.05110E-4 | 1.94710E-1 | 8.20380E-2 | 5.20330E+2 | 5.82430E-8 | 0.00000E+0 |
| 2600 | 1.08120E-4 | 1.87220E-1 | 8.43870E-2 | 5.20330E+2 | 1.89530E-8 | 0.00000E+0 |
| 2700 | 1.11100E-4 | 1.80290E-1 | 8.67140E-2 | 5.20330E+2 | 2.37470E-7 | 0.00000E+0 |
| 2800 | 1.14050E-4 | 1.73850E-1 | 8.76190E-2 | 5.20330E+2 | 2.30150E-6 | 0.00000E+0 |
| 2900 | 1.16980E-4 | 1.67860E-1 | 8.93010E-2 | 5.20330E+2 | 1.35770E-5 | 0.00000E+0 |
| 3000 | 1.19870E-4 | 1.62260E-1 | 9.25610E-2 | 5.20330E+2 | 4.69560E-5 | 0.00000E+0 |
| 3100 | 1.22740E-4 | 1.57030E-1 | 9.37980E-2 | 5.20330E+2 | 1.25460E-4 | 0.00000E+0 |
| 3200 | 1.25570E-4 | 1.52120E-1 | 9.60140E-2 | 5.20330E+2 | 2.99160E-4 | 0.00000E+0 |
| 3300 | 1.28370E-4 | 1.47510E-1 | 9.71210E-2 | 5.20330E+2 | 6.68070E-4 | 0.00000E+0 |
| 3400 | 1.31140E-4 | 1.43170E-1 | 9.87400E-2 | 5.20330E+2 | 1.42150E-3 | 0.00000E+0 |
| 3500 | 1.33890E-4 | 1.39080E-1 | 1.01160E-1 | 5.20330E+2 | 2.90350E-3 | 0.00000E+0 |
| 3600 | 1.36600E-4 | 1.35220E-1 | 1.02090E-1 | 5.20330E+2 | 5.71770E-3 | 0.00000E+0 |
| 3700 | 1.39280E-4 | 1.31570E-1 | 1.04040E-1 | 5.20330E+2 | 1.08880E-2 | 0.00000E+0 |
| 3800 | 1.41930E-4 | 1.28100E-1 | 1.07400E-1 | 5.20330E+2 | 2.00970E-2 | 0.00000E+0 |
| 3900 | 1.44550E-4 | 1.24820E-1 | 1.08950E-1 | 5.20330E+2 | 3.60350E-2 | 0.00000E+0 |
| 4000 | 1.47150E-4 | 1.21700E-1 | 1.11820E-1 | 5.20330E+2 | 6.28830E-2 | 0.00000E+0 |
| 4100 | 1.49720E-4 | 1.18730E-1 | 1.12190E-1 | 5.20330E+2 | 1.07000E-1 | 0.00000E+0 |
| 4200 | 1.52260E-4 | 1.15900E-1 | 1.15350E-1 | 5.20330E+2 | 1.77810E-1 | 0.00000E+0 |
| 4300 | 1.54770E-4 | 1.13210E-1 | 1.17200E-1 | 5.20330E+2 | 2.89000E-1 | 0.00000E+0 |
| 4400 | 1.57260E-4 | 1.10640E-1 | 1.18680E-1 | 5.20340E+2 | 4.60040E-1 | 0.00000E+0 |
| 4500 | 1.59720E-4 | 1.08180E-1 | 1.21400E-1 | 5.20340E+2 | 7.18320E-1 | 0.00000E+0 |
| 4600 | 1.62160E-4 | 1.05830E-1 | 1.22520E-1 | 5.20350E+2 | 1.10100E+0 | 0.00000E+0 |
| 4700 | 1.64580E-4 | 1.03580E-1 | 1.25530E-1 | 5.20360E+2 | 1.65870E+0 | 0.00000E+0 |

**Table XI: Continued**

| 4800 | 1.66970E-4 | 1.01420E-1 | 1.28180E-1 | 5.20380E+2 | 2.45840E+0 | 0.00000E+0 |
|------|-----------|-----------|-----------|-----------|-----------|-----------|
| 4900 | 1.69340E-4 | 9.93480E-2 | 1.29730E-1 | 5.20410E+2 | 3.58820E+0 | 0.00000E+0 |
| 5000 | 1.71690E-4 | 9.73610E-2 | 1.32030E-1 | 5.20450E+2 | 5.16150E+0 | 1.80000E-1 |
| 5100 | 1.74020E-4 | 9.54520E-2 | 1.35040E-1 | 5.20500E+2 | 7.06100E+0 | 2.38500E-1 |
| 5200 | 1.76320E-4 | 9.36170E-2 | 1.36930E-1 | 5.20570E+2 | 9.77310E+0 | 3.39200E-1 |
| 5300 | 1.78610E-4 | 9.18500E-2 | 1.38850E-1 | 5.20660E+2 | 1.33210E+1 | 5.13200E-1 |
| 5400 | 1.80880E-4 | 9.01490E-2 | 1.40290E-1 | 5.20790E+2 | 1.78830E+1 | 8.19500E-1 |
| 5500 | 1.83140E-4 | 8.85100E-2 | 1.43780E-1 | 5.20950E+2 | 2.36470E+1 | 1.37000E+0 |
| 5600 | 1.85370E-4 | 8.69300E-2 | 1.45820E-1 | 5.21160E+2 | 3.08050E+1 | 2.37600E+0 |
| 5700 | 1.87590E-4 | 8.54040E-2 | 1.47940E-1 | 5.21430E+2 | 3.95420E+1 | 4.24300E+0 |
| 5800 | 1.89790E-4 | 8.39320E-2 | 1.50150E-1 | 5.21780E+2 | 5.00280E+1 | 7.73800E+0 |
| 5900 | 1.91980E-4 | 8.25090E-2 | 1.52480E-1 | 5.22210E+2 | 6.24120E+1 | 1.42900E+1 |
| 6000 | 1.94150E-4 | 8.11330E-2 | 1.54940E-1 | 5.22760E+2 | 7.68210E+1 | 2.65000E+1 |
| 6100 | 1.96310E-4 | 7.98030E-2 | 1.57560E-1 | 5.23440E+2 | 9.33640E+1 | 4.29800E+1 |
| 6200 | 1.98450E-4 | 7.85150E-2 | 1.60370E-1 | 5.24270E+2 | 1.12140E+2 | 6.93900E+1 |
| 6300 | 2.00580E-4 | 7.72680E-2 | 1.63780E-1 | 5.25290E+2 | 1.33240E+2 | 1.11500E+2 |
| 6400 | 2.02700E-4 | 7.60590E-2 | 1.66630E-1 | 5.26520E+2 | 1.56790E+2 | 1.78400E+2 |
| 6500 | 2.04810E-4 | 7.48880E-2 | 1.71120E-1 | 5.28010E+2 | 1.82900E+2 | 2.83800E+2 |
| 6600 | 2.06900E-4 | 7.37520E-2 | 1.73880E-1 | 5.29800E+2 | 2.11740E+2 | 4.48800E+2 |
| 6700 | 2.08990E-4 | 7.26490E-2 | 1.77930E-1 | 5.31930E+2 | 2.43480E+2 | 7.05600E+2 |
| 6800 | 2.11060E-4 | 7.15780E-2 | 1.82290E-1 | 5.34450E+2 | 2.78310E+2 | 1.10200E+3 |
| 6900 | 2.13120E-4 | 7.05380E-2 | 1.86960E-1 | 5.37420E+2 | 3.16440E+2 | 1.71000E+3 |
| 7000 | 2.15170E-4 | 6.95270E-2 | 1.91970E-1 | 5.40910E+2 | 3.58080E+2 | 2.63400E+3 |
| 7100 | 2.17210E-4 | 6.85440E-2 | 1.97340E-1 | 5.44980E+2 | 4.03420E+2 | 4.00400E+3 |
| 7200 | 2.19250E-4 | 6.75870E-2 | 2.03080E-1 | 5.49710E+2 | 4.52610E+2 | 6.03900E+3 |
| 7300 | 2.21270E-4 | 6.66560E-2 | 2.09220E-1 | 5.55180E+2 | 5.05790E+2 | 9.04300E+3 |
| 7400 | 2.23280E-4 | 6.57490E-2 | 2.15780E-1 | 5.61480E+2 | 5.63040E+2 | 1.34400E+4 |
| 7500 | 2.25290E-4 | 6.48650E-2 | 2.22770E-1 | 5.68590E+2 | 6.24400E+2 | 1.98200E+4 |
| 7600 | 2.27290E-4 | 6.40030E-2 | 2.30250E-1 | 5.76780E+2 | 6.89840E+2 | 2.90200E+4 |
| 7700 | 2.29270E-4 | 6.31620E-2 | 2.38210E-1 | 5.85870E+2 | 7.59300E+2 | 4.21800E+4 |
| 7800 | 2.31250E-4 | 6.23420E-2 | 2.46740E-1 | 5.96540E+2 | 8.32640E+2 | 6.08400E+4 |
| 7900 | 2.33220E-4 | 6.15400E-2 | 2.55840E-1 | 6.08400E+2 | 9.09720E+2 | 8.71200E+4 |
| 8000 | 2.35180E-4 | 6.07570E-2 | 2.65520E-1 | 6.21330E+2 | 9.90340E+2 | 1.23800E+5 |
| 8100 | 2.37130E-4 | 5.99910E-2 | 2.75890E-1 | 6.36550E+2 | 1.07420E+3 | 1.74500E+5 |
| 8200 | 2.39060E-4 | 5.92410E-2 | 2.86950E-1 | 6.53190E+2 | 1.16120E+3 | 2.44100E+5 |
| 8300 | 2.40990E-4 | 5.85070E-2 | 2.98730E-1 | 6.71700E+2 | 1.25100E+3 | 3.38900E+5 |
| 8400 | 2.42900E-4 | 5.77880E-2 | 3.11370E-1 | 6.93150E+2 | 1.34330E+3 | 4.67300E+5 |
| 8500 | 2.44800E-4 | 5.70830E-2 | 3.24740E-1 | 7.15150E+2 | 1.43780E+3 | 6.39700E+5 |

**Table XI: Continued**

| | | | | | |
|---|---|---|---|---|---|
| 8600 | 2.46680E-4 | 5.63910E-2 | 3.38950E-1 | 7.40240E+2 | 1.53430E+3 | 8.69500E+5 |
| 8700 | 2.48550E-4 | 5.57110E-2 | 3.54030E-1 | 7.67840E+2 | 1.63260E+3 | 1.17400E+6 |
| 8800 | 2.50400E-4 | 5.50430E-2 | 3.70010E-1 | 7.98130E+2 | 1.73240E+3 | 1.57300E+6 |
| 8900 | 2.52220E-4 | 5.43870E-2 | 3.87100E-1 | 8.33590E+2 | 1.83360E+3 | 2.09500E+6 |
| 9000 | 2.54020E-4 | 5.37400E-2 | 4.04980E-1 | 8.67850E+2 | 1.93580E+3 | 2.77000E+6 |
| 9100 | 2.55790E-4 | 5.31030E-2 | 4.23850E-1 | 9.07330E+2 | 2.03900E+3 | 3.63800E+6 |
| 9200 | 2.57540E-4 | 5.24760E-2 | 4.43980E-1 | 9.53810E+2 | 2.14300E+3 | 4.74600E+6 |
| 9300 | 2.59240E-4 | 5.18560E-2 | 4.64890E-1 | 9.97240E+2 | 2.24760E+3 | 6.15100E+6 |
| 9400 | 2.60900E-4 | 5.12440E-2 | 4.87220E-1 | 1.05300E+3 | 2.35280E+3 | 7.92100E+6 |
| 9500 | 2.62520E-4 | 5.06390E-2 | 5.10250E-1 | 1.10270E+3 | 2.45840E+3 | 1.01400E+7 |
| 9600 | 2.64080E-4 | 5.00400E-2 | 5.34860E-1 | 1.16870E+3 | 2.56430E+3 | 1.28900E+7 |
| 9700 | 2.65590E-4 | 4.94470E-2 | 5.60060E-1 | 1.22540E+3 | 2.67050E+3 | 1.62900E+7 |
| 9800 | 2.67020E-4 | 4.88590E-2 | 5.87010E-1 | 1.30300E+3 | 2.77690E+3 | 2.04500E+7 |
| 9900 | 2.68380E-4 | 4.82760E-2 | 6.14430E-1 | 1.36710E+3 | 2.88340E+3 | 2.55300E+7 |
| 10000 | 2.69650E-4 | 4.76960E-2 | 6.43760E-1 | 1.45770E+3 | 2.99000E+3 | 3.16800E+7 |
| 10100 | 2.70830E-4 | 4.71200E-2 | 6.73410E-1 | 1.52940E+3 | 3.09660E+3 | 3.90800E+7 |
| 10200 | 2.71890E-4 | 4.65460E-2 | 7.05170E-1 | 1.63450E+3 | 3.20330E+3 | 4.79200E+7 |
| 10300 | 2.72840E-4 | 4.59750E-2 | 7.38210E-1 | 1.73330E+3 | 3.30990E+3 | 5.84400E+7 |
| 10400 | 2.73650E-4 | 4.54060E-2 | 7.71220E-1 | 1.81610E+3 | 3.41650E+3 | 7.08500E+7 |
| 10500 | 2.74310E-4 | 4.48380E-2 | 8.06680E-1 | 1.94690E+3 | 3.52310E+3 | 8.54300E+7 |
| 10600 | 2.74810E-4 | 4.42710E-2 | 8.43440E-1 | 2.06560E+3 | 3.62950E+3 | 1.02400E+8 |
| 10700 | 2.75140E-4 | 4.37040E-2 | 8.79710E-1 | 2.15910E+3 | 3.73590E+3 | 1.22200E+8 |
| 10800 | 2.75270E-4 | 4.31370E-2 | 9.18820E-1 | 2.31980E+3 | 3.84220E+3 | 1.45000E+8 |
| 10900 | 2.75190E-4 | 4.25700E-2 | 9.59190E-1 | 2.46030E+3 | 3.94840E+3 | 1.71100E+8 |
| 11000 | 2.74890E-4 | 4.20030E-2 | 1.00080E+0 | 2.60870E+3 | 4.05440E+3 | 2.00900E+8 |
| 11100 | 2.74350E-4 | 4.14340E-2 | 1.04110E+0 | 2.71320E+3 | 4.16030E+3 | 2.34700E+8 |
| 11200 | 2.73550E-4 | 4.08640E-2 | 1.08480E+0 | 2.92210E+3 | 4.26600E+3 | 2.72800E+8 |
| 11300 | 2.72480E-4 | 4.02930E-2 | 1.12970E+0 | 3.09410E+3 | 4.37160E+3 | 3.15500E+8 |
| 11400 | 2.71130E-4 | 3.97200E-2 | 1.17570E+0 | 3.27450E+3 | 4.47700E+3 | 3.63200E+8 |
| 11500 | 2.69470E-4 | 3.91450E-2 | 1.21930E+0 | 3.38540E+3 | 4.58220E+3 | 4.16200E+8 |
| 11600 | 2.67510E-4 | 3.85680E-2 | 1.26700E+0 | 3.65030E+3 | 4.68720E+3 | 4.74600E+8 |
| 11700 | 2.65240E-4 | 3.79900E-2 | 1.31560E+0 | 3.85480E+3 | 4.79200E+3 | 5.38800E+8 |
| 11800 | 2.62650E-4 | 3.74100E-2 | 1.36500E+0 | 4.06760E+3 | 4.89650E+3 | 6.08800E+8 |
| 11900 | 2.59730E-4 | 3.68280E-2 | 1.41510E+0 | 4.28840E+3 | 5.00080E+3 | 6.85000E+8 |
| 12000 | 2.56460E-4 | 3.62430E-2 | 1.46150E+0 | 4.39420E+3 | 5.10490E+3 | 7.67300E+8 |
| 12100 | 2.52890E-4 | 3.56580E-2 | 1.51250E+0 | 4.73920E+3 | 5.20860E+3 | 8.55900E+8 |
| 12200 | 2.49000E-4 | 3.50720E-2 | 1.56390E+0 | 4.98120E+3 | 5.31200E+3 | 9.50600E+8 |
| 12300 | 2.44800E-4 | 3.44850E-2 | 1.61550E+0 | 5.22980E+3 | 5.41500E+3 | 1.05200E+9 |

**Table XI: Continued**

| | | | | | | |
|---|---|---|---|---|---|---|
| 12400 | 2.40300E-4 | 3.38970E-2 | 1.66730E+0 | 5.48410E+3 | 5.51760E+3 | 1.15900E+9 |
| 12500 | 2.35520E-4 | 3.33100E-2 | 1.71910E+0 | 5.74360E+3 | 5.61990E+3 | 1.27100E+9 |
| 12600 | 2.30480E-4 | 3.27230E-2 | 1.77070E+0 | 6.00730E+3 | 5.72160E+3 | 1.39000E+9 |
| 12700 | 2.25160E-4 | 3.21340E-2 | 1.81660E+0 | 6.06450E+3 | 5.82330E+3 | 1.51400E+9 |
| 12800 | 2.19660E-4 | 3.15490E-2 | 1.86710E+0 | 6.52520E+3 | 5.92420E+3 | 1.64300E+9 |
| 12900 | 2.13960E-4 | 3.09670E-2 | 1.91700E+0 | 6.79420E+3 | 6.02450E+3 | 1.77700E+9 |
| 13000 | 2.08110E-4 | 3.03870E-2 | 1.96590E+0 | 7.06250E+3 | 6.12430E+3 | 1.91400E+9 |
| 13100 | 2.02120E-4 | 2.98100E-2 | 2.01370E+0 | 7.32860E+3 | 6.22350E+3 | 2.05600E+9 |
| 13200 | 1.96030E-4 | 2.92380E-2 | 2.06010E+0 | 7.59070E+3 | 6.32200E+3 | 2.20100E+9 |
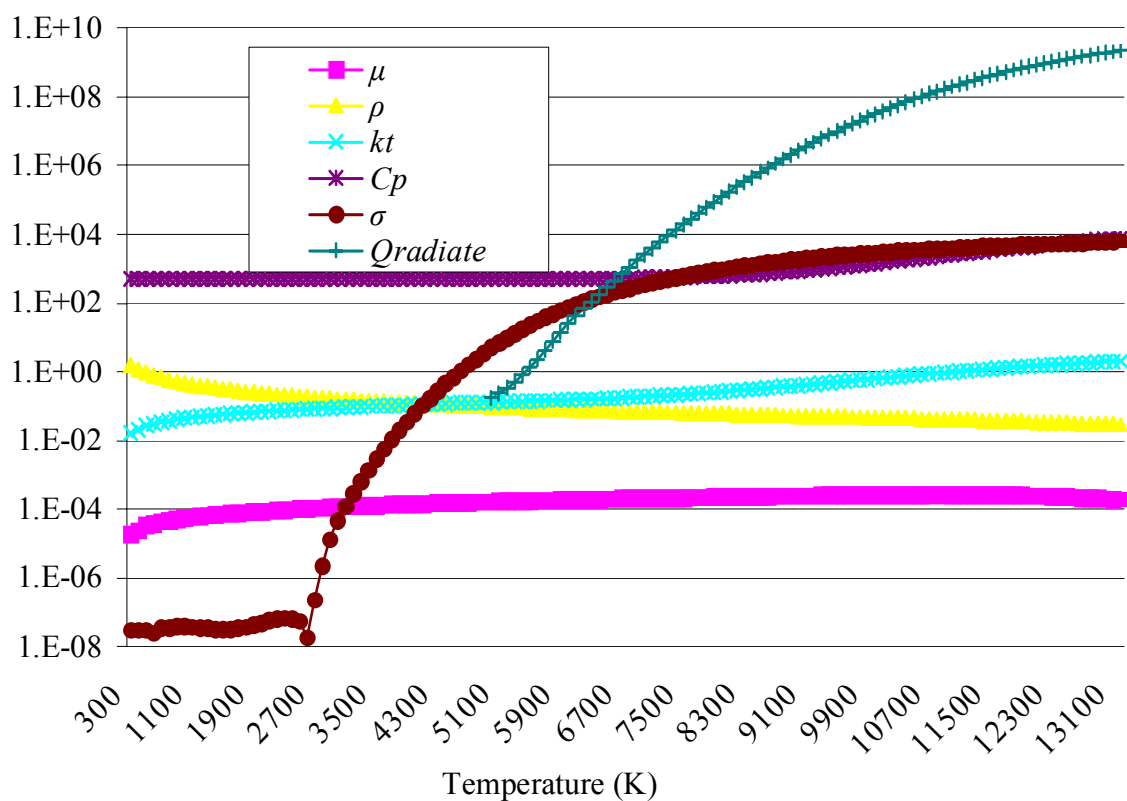


**Figure 29: Argon Properties (Units in Table X)**

## APPENDIX C: SOURCE CODE

The following tables list the different UDF codes written in C++ language. There are 28 different user defined functions in 2-D and 43 in the 3-D case. The 2-D and 3-D code is 783 and 700 lines respectively including commentary.

**Table XII: 2-D User Defined Functions**

|   | Name | Type of UDF - Description |
|---|------|--------------------------|
| 1 | On_Loading_UDS | DEFINE_EXECUTE_ON_LOADING - Defines and gives names to the imaginary and real parts of the user-defined scalar functions |
| 2 | On_Loading_UDM | DEFINE_EXECUTE_ON_LOADING - Defines and gives names to eight user-defined memory variables |
| 3 | Input_Data | DEFINE_EXECUTE_ON_LOADING - Inputs data into memory for the argon properties listed in appendix B |
| 4 | Get_Fields | DEFINE_ON_DEMAND - Computes and stores the values of the real and imaginary components of magnetic field into memory variables for data processing |
| 5 | Get_Force | DEFINE_ON_DEMAND - Computes and stores the Lorentz force per unit volume from the magnetic fields into memory variables for data processing |
| 6 | Get_Joule | DEFINE_ON_DEMAND - Calculates the joule heating + radiative cooling per unit volume and stores into memory for data processing |
| 7 | Get_Joule_Alone | DEFINE_ON_DEMAND - Calculates the joule heating per unit volume and stores into memory for data processing |
| 8 | Get_Sigma | DEFINE_ON_DEMAND - Calculates the conductivity from Input_Data as a continuous function of temperature for data processing |
| 9 | Argon_Density | DEFINE_PROPERTY - This UDF Calculates the density from Input_Data as a continuous function of temperature for iteration |
| 10 | Argon_TherCond | DEFINE_PROPERTY - This UDF Calculates the thermal conductivity from Input_Data as a continuous function of temperature for iteration |
| 11 | Argon_Viscosity | DEFINE_PROPERTY - This UDF Calculates the density from Input_Data as a continuous function of temperature for iteration |

**Table XII: Continued**

| 12 | RPlasmaSource | DEFINE_SOURCE - Calculates the source term defined as $A_{R\theta}$ in the plasma region |
|---|---|---|
| 13 | IPlasmaSource | DEFINE_SOURCE - Calculates the source term defined as $A_{I\theta}$ in the plasma region |
| 14 | ROutsideSource | DEFINE_SOURCE - Calculates the source term defined as $A_{R\theta}$ in the walls and outside regions |
| 15 | IOutsideSource | DEFINE_SOURCE - Calculates the source term defined as $A_{I\theta}$ in the walls and outside regions |
| 16 | RCoilSource | DEFINE_SOURCE - Calculates the source term defined as $A_{R\theta}$ in the coil regions |
| 17 | ICoilSource | DEFINE_SOURCE - Calculates the source term defined as $A_{I\theta}$ in the coil regions |
| 18 | Joule_Heating | DEFINE_SOURCE - Calculates the joule heating + radiative cooling per unit volume as a continuous function of temperature for iteration |
| 19 | Outside_Energy | DEFINE_SOURCE - Calculates the artificial regulating source to keep the outside region at 300K |
| 20 | Plasma_Energy | DEFINE_SOURCE - Calculates the artificial heating source to assist in initializing the magnetic field |
| 21 | Axial_Source | DEFINE_SOURCE - Calculates the axial component source term of Lorentz force per unit volume as a continuous function of temperature for iteration |
| 22 | Radial_Source | DEFINE_SOURCE - Calculates the radial component source term of Lorentz force per unit volume as a continuous function of temperature for iteration |
| 23 | RtopDPBCflux | DEFINE_PROFILE - This calculates the real component of the dipole boundary condition along the top wall |
| 24 | ItopDPBCflux | DEFINE_PROFILE - This calculates the imaginary component of the dipole boundary condition along the top wall |
| 25 | RrightDPBCflux | DEFINE_PROFILE - This calculates the real component of the dipole boundary condition along the right wall |
| 26 | IrightDPBCflux | DEFINE_PROFILE - This calculates the imaginary component of the dipole boundary condition along the right wall |
| 27 | RleftDPBCflux | DEFINE_PROFILE - This calculates the real component of the dipole boundary condition along the left wall |
| 28 | IleftDPBCflux | DEFINE_PROFILE - This calculates the imaginary component of the dipole boundary condition along the left wall |

**Table XIII: 3-D User Defined Functions**

|    | Name | Type of UDF- Description |
|----|------|-------------------------|
| 1  | Sigma | DOUBLE_FUNCTION- Calculates a 2nd order continuous function for conductivity for the scalar potential source term |
| 2  | On_Loading_UDS | DEFINE_EXECUTE_ON_LOADING- Defines and gives names to the imaginary and real parts of the user-defined scalar functions |
| 3  | On_Loading_UDM | DEFINE_EXECUTE_ON_LOADING- Defines and gives names to eight user-defined memory variables |
| 4  | Input_Data | DEFINE_EXECUTE_ON_LOADING- Inputs data into memory for the argon properties listed in appendix B |
| 5  | Get_Fields_Force | DEFINE_ON_DEMAND- Computes and stores the values of the real and imaginary components of magnetic field and forces into memory variables for data processing |
| 6  | Get_Joule | DEFINE_ON_DEMAND- Calculates the joule heating + radiative cooling per unit volume and stores into memory for data processing |
| 7  | Get_Joule_Alone | DEFINE_ON_DEMAND- Calculates the joule heating per unit volume and stores into memory for data processing |
| 8  | Test_Sigma | DEFINE_ON_DEMAND- Calculates the conductivity from Input_Data to verify Input_Data |
| 9  | Argon_Density | DEFINE_PROPERTY- This UDF Calculates the density from Input_Data as a continuous function of temperature for iteration |
| 10 | Argon_TherCond | DEFINE_PROPERTY- This UDF Calculates the thermal conductivity from Input_Data as a continuous function of temperature for iteration |
| 11 | Argon_Viscosity | DEFINE_PROPERTY- This UDF Calculates the density from Input_Data as a continuous function of temperature for iteration |
| 12 | Sigma_B_F | DEFINE_ADJUST- At the beginning of each iteration the fields and forces are calculated once to global variables to reduce commands |
| 13 | AdjustCurrent | DEFINE_ADJUST- This UDF calculates if the current should be adjusted and adjusts the modeled current |
| 14 | A_R_X_Coil | DEFINE_SOURCE- Calculates the source term defined for the Real X Component of the vector potential in the coil region |
| 15 | A_R_Y_Coil | DEFINE_SOURCE- Calculates the source term defined for the Real Y Component of the vector potential in the coil region |
| 16 | A_R_Z_Coil | DEFINE_SOURCE- Calculates the source term defined for the Real Z Component of the vector potential in the coil region |

**Table XIII: Continued**

| 17 | A_I_X_Coil | DEFINE_SOURCE- Calculates the source term defined for the Imaginary X Component of the vector potential in the coil region |
|----|------------|---------------------------------------------------------------------------------------------------------------------------|
| 18 | A_I_Y_Coil | DEFINE_SOURCE- Calculates the source term defined for the Imaginary Y Component of the vector potential in the coil region |
| 19 | A_I_Z_Coil | DEFINE_SOURCE- Calculates the source term defined for the Imaginary Z Component of the vector potential in the coil region |
| 20 | A_R_X_Plasma | DEFINE_SOURCE- Calculates the source term defined for the Real X Component of the vector potential in the plasma region |
| 21 | A_R_Y_Plasma | DEFINE_SOURCE- Calculates the source term defined for the Real Y Component of the vector potential in the plasma region |
| 22 | A_R_Z_Plasma | DEFINE_SOURCE- Calculates the source term defined for the Real Z Component of the vector potential in the plasma region |
| 23 | A_I_X_Plasma | DEFINE_SOURCE- Calculates the source term defined for the Imaginary X Component of the vector potential in the plasma region |
| 24 | A_I_Y_Plasma | DEFINE_SOURCE- Calculates the source term defined for the Imaginary Y Component of the vector potential in the plasma region |
| 25 | A_I_Z_Plasma | DEFINE_SOURCE- Calculates the source term defined for the Imaginary Z Component of the vector potential in the plasma region |
| 26 | A_R_X_Outside | DEFINE_SOURCE- Calculates the source term defined for the Real X Component of the vector potential in the outside region |
| 27 | A_R_Y_Outside | DEFINE_SOURCE- Calculates the source term defined for the Real Y Component of the vector potential in the outside region |
| 28 | A_R_Z_Outside | DEFINE_SOURCE- Calculates the source term defined for the Real Z Component of the vector potential in the outside region |
| 29 | A_I_X_Outside | DEFINE_SOURCE- Calculates the source term defined for the Imaginary X Component of the vector potential in the outside region |
| 30 | A_I_Y_Outside | DEFINE_SOURCE- Calculates the source term defined for the Imaginary Y Component of the vector potential in the outside region |
| 31 | A_I_Z_Outside | DEFINE_SOURCE- Calculates the source term defined for the Imaginary Z Component of the vector potential in the outside region |
| 32 | Phi_R_Coil | DEFINE_SOURCE- Calculates the source term defined for the Real Component of the scalar potential in the Coil region |

**Table XIII: Continued**

| 33 | Phi_I_Coil | DEFINE_SOURCE- Calculates the source term defined for the Imaginary Component of the scalar potential in the Coil region |
|---|---|---|
| 34 | Phi_R_Plasma | DEFINE_SOURCE- Calculates the source term defined for the Real Component of the scalar potential in the plasma region |
| 35 | Phi_I_Plasma | DEFINE_SOURCE- Calculates the source term defined for the Imaginary Component of the scalar potential in the plasma region |
| 36 | Phi_R_Outside | DEFINE_SOURCE- Calculates the source term defined for the Real Component of the scalar potential in the outside region |
| 37 | Phi_I_Outside | DEFINE_SOURCE- Calculates the source term defined for the Imaginary Component of the scalar potential in the outside region |
| 38 | Joule_Heating | DEFINE_SOURCE- Calculates the joule heating + radiative cooling per unit volume as a continuous function of temperature for iteration |
| 39 | Outside_Energy | DEFINE_SOURCE- Calculates the artificial regulating source to keep the outside region at 300K |
| 40 | Plasma_Energy | DEFINE_SOURCE- Calculates the artificial heating source to assist in initializing the magnetic field |
| 41 | X_Source | DEFINE_SOURCE- Calculates the X component source term of Lorentz force per unit volume as a continuous function of temperature for iteration |
| 42 | Y_Source | DEFINE_SOURCE- Calculates the Y component source term of Lorentz force per unit volume as a continuous function of temperature for iteration |
| 43 | Z_Source | DEFINE_SOURCE- Calculates the Z component source term of Lorentz force per unit volume as a continuous function of temperature for iteration |

**APPENDIX D: CHARACTERISTIC MESH LENGTHS**

The following two figures are simply a graphical representation of Table VII and Table VIII.
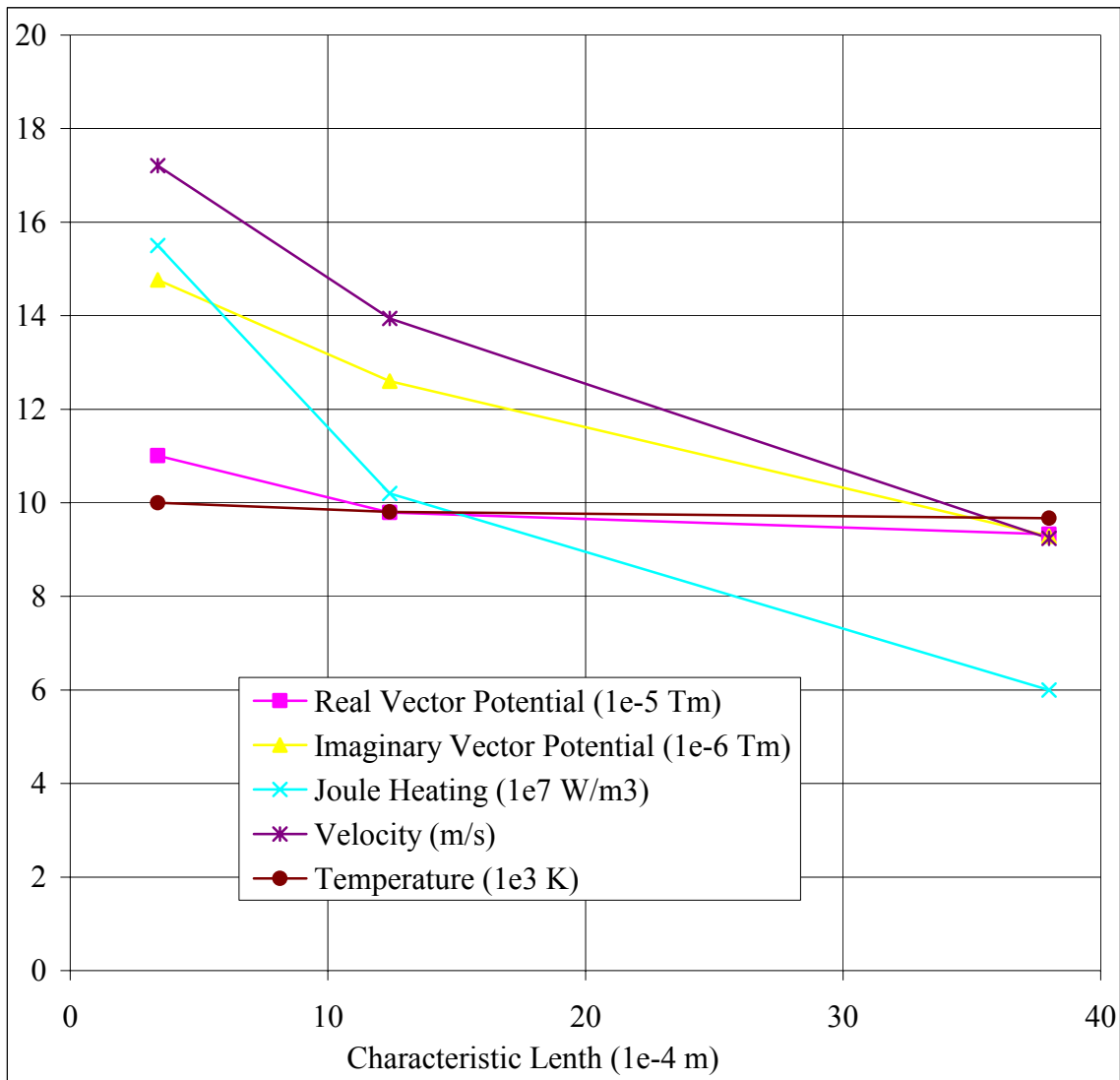


**Figure 30: Flow Maxima verses Mesh Characteristic Length for Set Currents**
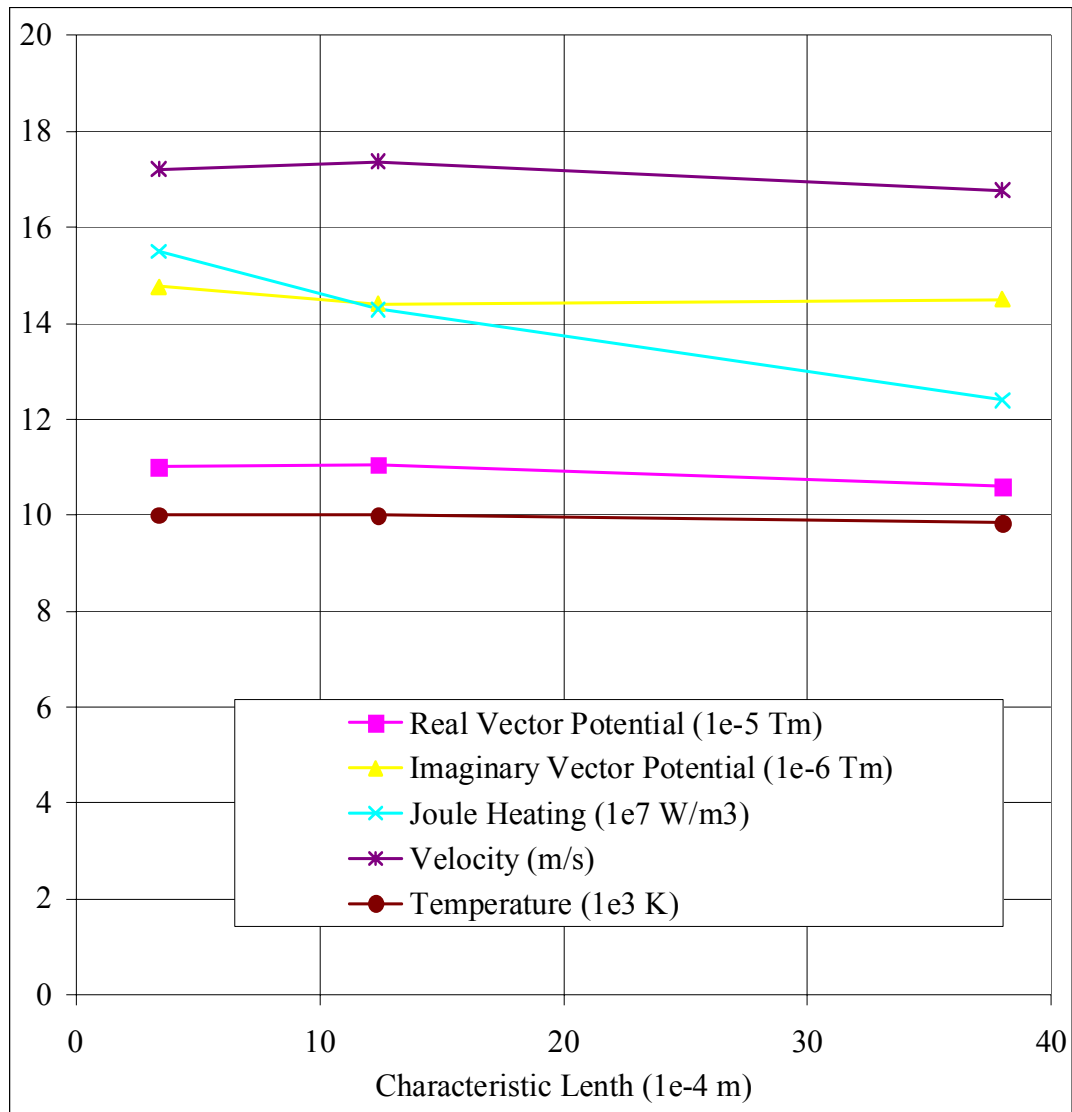
**Figure 31: Flow Maxima verses Mesh Characteristic Length for Set Power**

**VITA**

| | |
|---|---|
| Name: | Eddie Frank (Trey) Holik III |
| Address: | Department of Physics, c/o Dr. Peter M. McIntyre, Texas A&M University, 4242 TAMU, College Station, TX 77843-4242 |
| Email: | eholik@physics.tamu.edu |
| Education: | B.S., Physics & Mathematics, Angelo State University 2006 M.S., Physics, Texas A&M University 2008 |